Materials Today Bio 16 (2022) 100395

Contents lists available at ScienceDirect

Materials Today Bio

journal homepage: www.journals.elsevier.com/materials-today-bio

Antibacterial coaxial hydro-membranes accelerate diabetic wound healing by tuning surface immunomodulatory functions

Wei Zhang [a,b,1], Sizhan Xia [a,b,1], Tingting Weng [a,b], Min Yang [a,b], Jiaming Shao [a,b], Manjia Zhang [c], Jialiang Wang [a,b], Pengqing Xu [a,b], Jintao Wei [b,d,e,f], Ronghua Jin [a,b], Meirong Yu [b], Zhongtao Zhang [a,b], Chunmao Han [a,b], Xingang Wang [a,b,*]

[a] Department of Burns and Wound Care Center, The Second Affiliated Hospital of Zhejiang University College of Medicine, Hangzhou, 310000, China
[b] The Key Laboratory of the Diagnosis and Treatment of Severe Trauma and Burn of Zhejiang Province, Hangzhou 310000, China
[c] The First Clinical Medical College, Zhejiang Chinese Medical University, Hangzhou, 310053, China
[d] Department of Emergency Medicine, The Second Affiliated Hospital of Zhejiang University College of Medicine, Hangzhou, 310000, China
[e] Institute of Emergency Medicine, Zhejiang University, Hangzhou, 310000, China
[f] Zhejiang Province Clinical Research Center for Emergency and Critical Care Medicine, Jiefang Road 88, Hangzhou, 310009, China

ARTICLE INFO

Keywords:
Advanced glycation end products
Immunomodulatory biomaterials
Macrophage polarization
Anti-inflammatory activity
Diabetic wound healing

ABSTRACT

Diabetic foot ulcers, typical non-healing wounds, represent a severe clinical problem. Advanced glycation end-products (AGEs), which create a prolonged pro-inflammatory micro-environment in defective sites, can be responsible for refractoriness of these ulcers. Macrophages are polarized to the M2 phenotype to facilitate the transition from a pro-inflammatory microenvironment to an anti-inflammatory microenvironment, which has been demonstrated to be an effective way to accelerate diabetic wound closure. Herein, we developed coaxial hydro-membranes mimicking the extracellular matrix structure that are capable of anti-inflammatory and anti-bacterial functions for diabetic wound repair. These fibrous membranes maintain a moist microenvironment to support cell proliferation. Macrophages grow in an elongated shape on the surface of the fibrous membranes. The fibrous membranes effectively impaired macrophage AGE-induced M1 polarization and induced macrophage polarization towards the M2 phenotype. The effects of the fibrous membranes on the interactions between macrophages and repair cells under a diabetic condition were also investigated. Furthermore, *in vivo* results from a full-thickness diabetic wound model confirmed the potential of the coaxial hydro-membranes to accelerate wound healing. This study's results indicate that the developed bioactive anti-inflammatory and antibacterial wound dressing can affect AGE-induced macrophage activation and crosstalk between macrophages and fibroblasts for treating diabetic wounds.

1. Introduction

Diabetes mellitus affects more than 300 million patients worldwide and is one of the most challenging epidemics [1]. One of the most serious complications associated with diabetes is chronic non-healing wounds. Within the diabetic hyperglycaemic environment, advanced glycation end-products (AGEs) act as one of the major factors underlying the pathology of delayed healing of diabetic wounds [2]. AGEs binding with receptor for AGEs (RAGE) induces intracellular generation of reactive oxygen species (ROS), which in turn results in the activation of the nuclear transcription factor, NF-κB, an inducer of pro-inflammatory gene expression [3]. Enhanced levels of AGEs persistently trigger pro-inflammatory signals by inducing macrophage M1 polarization which disturbs the transition from inflammation to the next proliferation stage in the healing of diabetic wounds [3–5]. Many studies have revealed that transformation of the macrophage phenotype is the central regulatory contributor that orchestrates the transitions among all phases of wound healing [6]. In the normal wound microenvironment, macrophages exhibit a pro-inflammatory phenotype (M1) during the early stage and then shift to an anti-inflammatory phenotype (M2) during the

* Corresponding author. Department of Burns & Wound Care Center, the Second Affiliated Hospital of Zhejiang University College of Medicine, Hangzhou, 310000, China.
E-mail address: wangxingang8157@zju.edu.cn (X. Wang).
[1] Wei Zhang and Sizhan Xia contributed equally to this paper.

https://doi.org/10.1016/j.mtbio.2022.100395
Received 23 June 2022; Received in revised form 4 August 2022; Accepted 6 August 2022
Available online 13 August 2022

later stage [7]. However, macrophages maintain a pro-inflammatory M1 phenotype in chronic diabetic wounds due to the presence of AGEs and secrete pro-inflammatory cytokines to sustain inflammation by recruiting new macrophages to the wound site and polarizing them to the M1 phenotype in a positive feedback loop [8]. Hence, modulation of macrophage polarization is key for diabetic wound healing [9]. Diabetic wounds are often accompanied by colonization of bacteria [10]. Some strategies, such as localized delivery of growth factors and drugs, have been used to inhibit M1 polarization [11,12]; however, due to the ease of inactivation, a short half-life, unsustainable action under physiological conditions, high cost and a long treatment time, the curative effect is insufficient and the proportion of non-responding patients remains high [13].

In addition to soluble factors, physical cues can affect the polarization of macrophages by controlling cell shape [14]. This phenomenon is based on the finding that macrophages sense biomaterial-mediated physical cues and convert them to biochemical and electrical signals by activating the integrin-mediated signaling pathway [15]. For example, spatial confinement downsizes the inflammatory response of macrophages [16]. A hydrophilic surface promotes an elongated shape in bone marrow-derived macrophages (BMDMs) [17]. Designed micro/-nanostructures can induce RAW 264.7 cells to adopt an M2-polarized morphology [18]. Many studies have demonstrated that surface physical cues, independent of chemical cues, regulate macrophage behaviours, such as polarization and the secretion of cytokines [19]. However, no study has reported that changes in surface modifications can convert AGE-mediated macrophage polarization to promote diabetic wound healing. More importantly, the details of biomaterial-mediated crosstalk between macrophages and fibroblasts remain unknown.

Micro/nanofibres are one of the most effective approaches for activating mechanotransduction of host cells, as they function similarly to the extracellular matrix (ECM) in providing a suitable microenvironment for the growth and migration of host cells [20]. Electrospinning technology has become an efficient process with which to produce micro/-nanofibres [21]. Electrospun fibres provide a high surface area and micropores, which allow for gaseous and fluid exchange [21]. Approved by the FDA, ε-polycaprolactone (PCL) presents one of the most commonly used biodegradable polymers for electrospinning technology. It is particularly lauded for its good physical and biological properties, including biocompatibility, low degradation rate, and good mechanical integrity [22]. Silver nanoparticles (AgNPs) are strong antibacterial agents [23]. Loading electrospun fibres with AgNPs has become an effective strategy to endow wound dressings with an antibacterial function for diabetic wound repair [24,25].

Gelatin-methacryloyl (GelMA) hydrogels absorb wound exudates and retain moisture, providing a moist environment to facilitate wound healing [26]. GelMA contains arginine-glycine-aspartic acid sequences, which promote cell attachment and proliferation [27,28]. However, inferior mechanical properties have hampered their application in wound healing, although the effects of biomaterial surface modifications of electrospun polymer scaffolds have been extensively studied [28]. Therefore, GelMA-modified electrospun fibres exhibit appropriate surface features that may be useful in regulating macrophage responses.

In this study, we hypothesized that suitable changes in biomaterial-mediated microenvironmental cues could override AGE-induced polarization of macrophages. We fabricated electrospun PCL fibres incorporated with AgNPs (Ag-PCL) to mimic the topology of the ECM and provide mechanical strength and antibacterial properties. Different layers of GelMA coating were used to change surface cues. We used an *in vitro* model in which macrophages were stimulated by AGEs to mimic the conditions near a diabetic wound, and Ag-PCL/GelMA membranes were used to stimulate BMDMs to explore their ability to induce macrophage elongation and synthesize cytokines. The effect and mechanism of the fibrous membranes involved in the crosstalk between macrophages and downstream fibroblasts were investigated. In addition, a diabetic full-thickness wound model was employed to evaluate the therapeutic effects of the Ag-PCL/GelMA membranes.

2. Materials and methods

2.1. Preparation of Ag-PCL/GelMA fibrous membranes

First, 25 g of gelatine was dissolved in 250 ml of phosphate buffer and stirred at 50 °C for 30 min. Then, 5 ml of methacrylic anhydride was added to the gelatine solution under intense stirring for 3 h. At the end of the reaction, dialysis was conducted four times (4 h each time) with a dialysis bag (3500 Da), and the solution was then lyophilized to obtain the product. The lyophilized GelMA foam was dissolved in phosphate-buffered saline (PBS) containing 0.3% lithium 2,4,6-trimethyl benzoyl phosphate as a photo-initiator at 40–50 °C for 30 min. The pH of the GelMA bio-ink was adjusted to 7.4 with 10 M NaOH solution.

PCL (average Mn 80,000) was purchased from Sigma-Aldrich (Sigma, USA). The obtained AgNPs were 20–40 nm in diameter (Huzheng Nano Technology Co., Ltd., China). A PCL solution (25% w/v) was prepared in a 3:1 (v/v) mixture of chloroform and methanol. AgNPs were added to the solution and stirred thoroughly to create a suspension for electrospinning with an Ag content of 50 ppm. The suspension was electrospun to form Ag-PCL fibrous membranes. The membranes were immersed in 3% GelMA solution for 10 s after which the mixture was photo-crosslinked. The membranes were washed in PBS, and monolayer GelMA-coated membranes were fabricated. These steps were repeated three times, to produce trilayer GelMA-coated membranes.

2.2. Scanning electron microscopy (SEM) observations

2.2.1. Topographical observations of fibrous membranes

After lyophilization for 24 h, samples were coated with gold-palladium in a Model E−1010 ion sputterer (Hitachi, Japan) for 4–5 min and visualized using a Hitachi Model SU-8010 scanning electron microscope (Philips XL30, Best, the Netherlands). To determine the mean diameter of the samples, 500 random fibres were selected and measured using ImageJ software (NIH, USA).

2.2.2. Morphological observations of macrophages cultured on the fibrous membranes

BMDMs at density of 10^4 cells/cm^2 were sparsely cultured on different fibrous membranes in the presence of 400 μg/ml AGEs for 24 h. The membranes were dehydrated through a gradient ethanol series of 30%, 50%, 70%, 90% and 100% for 10 min each step. The morphologies of the macrophages cultured on the different membranes were observed under a Hitachi Model SU-8010 scanning electron microscope.

2.3. Water contact angle measurements

To measure the hydrophilicity of the samples, the static water contact angle of a drop of deionized water on the sample surface was measured at room temperature using a goniometer (OCA20, DataPhysics Instruments GmBH, Germany). Briefly, 4-μl droplets of distilled water were dropped onto the surface of samples using a micro-syringe, with the procedure repeated three times for each sample. A photograph was taken after 5 s to measure the water contact angle using ImageJ software.

2.4. Water absorption and retention properties

The water absorption and retention properties of the fibres were measured according to a previous report [29]. The weight of the samples was recorded (W1). The samples were immersed in 30 ml of normal saline, distilled water and solution A for 2 h each solution. Then, the fibrous membranes were removed and hung for 2 min, and the weight of each sample was then recorded (W2). The water on the surface of the fibres was removed via centrifugation at 2000 r/min for 15 min and the weight of each sample was recorded (W3). The water absorption and water

retention rates were calculated using the following formula:

$$Water\ absorption\ rate = \frac{W2 - W1}{W1} \times 100\%$$

$$Water\ retention\ rate = \frac{W3 - W1}{W1} \times 100\%$$

2.5. Swelling ratio

Three samples from each group were immersed in PBS at 37 °C for 24 h and then lightly dried. The weights of the hydrated gels were measured (Wwet). The hydrated gels were freeze-dried for 24 h and weighed (Wdry). The swelling ratio (SR) was calculated using the equation:

$$Swelling\ ratio = \frac{Wwet - Wdry}{Wdry} \times 100\%$$

2.6. Surface pH

Fibrous membranes were moistened in PBS and incubated on a PBS-agarose gel at 37 °C (humidity >90%) to simulate dressing application [30]. The pH of the surface of the fibrous membranes contacting the agarose was detected using a meter.

2.7. Mechanical characterizations

The tensile strength of fibrous membranes was tested at 500 N with a 10 mm/min rate using a universal testing machine (AGX-PLUS, Shimadzu, Japan). Each sample was cut into a rectangle with thickness × width × length (0.1 × 2 × 15 mm). The stress-strain diagrams were acquired, and Young's modulus and tensile strength were calculated.

2.8. Antibacterial performance

Escherichia coli and *Staphylococcus aureus* were used for the evaluation of antibacterial activity. The bacteria were cultured in Luria Bertani (LB) medium until the optical density (OD) value reached 2.0. Fibrous membranes were incubated in the bacterial suspension for 12 h. The bacterial solution obtained was diluted with PBS to a concentration of 10^{-5}, and 100 μl of the solution was seeded in dishes containing LB medium. After overnight incubation at 37 °C, images of the LB dishes were captured, and the number of bacterial colonies was counted. The inhibitory rate (%) was calculated as $(a - b)/a \times 100\%$, where a and b refer to the colony numbers for the blank control and samples, respectively.

2.9. Cell isolation and culture

BMDMs were isolated from 4-week-old Sprague–Dawley (SD) rats. Briefly, bone marrow cells from the femurs and tibias were flushed out and cultured in complete alpha modified Eagle's medium (Gibco-BRL, Australia) with 25 ng/ml of macrophage colony-stimulating factor (M-CSF; R&D Systems, USA) for 5 d to differentiate into BMDMs. Rat primary fibroblasts were isolated from the skin of 8-week-old male SD rats and cultured in Dulbecco's modified Eagle's medium (Sigma, USA). All cell media were supplemented with 10% foetal bovine serum, 1% penicillin and 1% streptomycin. All cell cultures were maintained at 37 °C in an incubator under 5% humidified CO_2. The BMDMs were cultured in 24-well plates with 25 ng/ml M-CSF. After allowing the cells to adhere overnight, they were treated with 10 ng/ml lipopolysaccharide (LPS) or 400 μg/ml AGEs for an additional 24 h.

2.10. Cell adhesion

Cell adhesion was examined using TRITC-labelled phalloidin (YEASEN, China) and DAPI (Boster, China). Fibroblasts at density of 104 cells/cm2 cultured on fibrous membranes in a 24-well plate at different time points were fixed in 4% paraformaldehyde for 15 min. Then, TRITC-labelled phalloidin solution (1:100) with 1% bovine serum albumin was added, and the mixture was incubated for 30 min. DAPI was added followed by incubation for 30 min. The working solution was removed, and the samples were imaged under a fluorescence microscope (EU5888, Leica, Germany).

2.11. Cell viability

The viability of the fibroblasts in the fibrous membranes was investigated using the live/dead assay. In brief, the fibroblasts at density of 10^4 cells/cm^2 were cultured on different groups of fibrous membranes in a 24-well plate for 24 h before being stained with a live/dead assay kit (YEASEN, China) following the manufacturer's protocol. Images were taken using a fluorescent microscope (Tokyo, Japan).

2.12. Cell proliferation

Fibroblasts at density of 10^4 cells/cm^2 were seeded on membranes and cultured in 96-well plates in triplicate for 2, 4, 6 and 10 days. Cell proliferation was assessed using the Cell Counting Kit-8 (CCK-8) assay (Beyotime, China) according to the manufacturer's instructions. An enzyme-linked immunosorbent assay (ELISA) plate reader (Titertek, Finland) was used to determine the OD values of formazan at 450 nm in the different groups.

2.13. RNA extraction and quantitative polymerase chain reaction (PCR)

Fibroblasts at 10^4 cells/cm^2 were seeded on Ag-PCL, Monolayer, Bilayer, and Trilayer membranes and cultured in 12-well plates for 14 days. The membranes were first washed with cold PBS, then incubated with TRIzol reagent (Invitrogen, USA) for 10 min at 4 °C. Then, the collected suspension was centrifuged at 14,000×g for 5 min. The supernatant was separated, and isopropanol was added, after which the RNA was precipitated by centrifugation for 10 min at 15,000×g and 4 °C. The supernatant was separated, 1 ml of 75% ethanol was added to the RNA pellet, and the samples were centrifuged for 5 min at 15,000×g and 4 °C. The supernatant was separated, and the RNA pellet was air dried for ~10 min and dissolved in 30 μL of water treated with diethyl pyrocarbonate (DEPC). RNA concentration and purity were determined using the Nanodrop 2000 (Thermo Scientific, Waltham, Massachusetts, USA). Total RNA was reversed transcribed to cDNA using PrimeScript RT Master Mix (TaKaRa Biotechnology, Japan), according to the manufacturers' protocols. Real-time quantitative PCR was performed with the TB Green Premix Ex Taq kit (TaKaRa Biotechnology) to quantify mRNA levels on a StepOnePlus Real-Time PCR System (Applied Biosystems, USA), which were calculated by the $2 - \Delta\Delta Ct$ method. All reactions were performed under the following conditions: 95 °C for 60 s and 40 cycles of 95 °C for 10 s, 60 °C for 20 s and 72 °C for 20 s. GAPDH was used as the endogenous control. The primer sequences are listed in Table 1.

2.14. Analysis of BMDM morphology

The long and short axes of each BMDM were manually traced and measured using ImageJ software. The long axis was defined as the longest length of the cell, and the short axis was defined as the length across the nucleus in a direction perpendicular to the long axis. The ratio of the two axes was the elongation factor. The area of each cell was determined by tracing the cell outline.

2.15. Western blot analysis

Total protein was isolated from cultured cells using radioimmunoprecipitation assay lysis buffer (Thermo Fisher Scientific, USA)

Table 1
Primers of tested genes by quantitative polymerase chain reaction (qPCR).

Genes	Primers	Sequence (5′–3′)
GAPDH	Forward Reverse	5′-CGTGCCGCCTGGAGAAACCTG-3′, 5′-AGAGTGGGAGTTGCTGTTGAAGTCG-3′
COL1A1	Forward Reverse	5′-GAGCGGAGAGTACTGGATCG-3′, 5′-TAC TCGAACGGGAATCCATC-3
COL1A2	Forward Reverse	5′-TTGACCCTAACCAAGGATGC-3′, 5′-CACCCCTTCTGCGTTGTATT -3′
FAK	Forward Reverse	5′-ACTTGGACGCTGTATTGGAG-3′, 5′-CTGTTGCCTGTCTTCTGGAT-3′
FN	Forward Reverse	5′-GGAC ACTA TGCG GGTC ACTT GG-3′, 5′-TGCT GTTC GTAC ACGC TGGA GA-3′

Collagen type I α1 (COL1A1); Collagen type I α2 (COL1A2); Focal adhesion kinase (FAK); Fibronectin (FN).

at 4 °C for 30 min. Lysates were centrifuged at 12,000×*g* for 20 min, and the supernatants were collected. Proteins were separated via 8% sodium dodecyl sulphate-polyacrylamide gel electrophoresis and transferred to 0.22-μm polyvinylidene difluoride membranes (Millipore, USA). The membranes were blocked with 5% skim milk for 1 h and incubated at 4 °C overnight with the primary antibodies rabbit anti–NF–κB p65 (1:1000, Cell Signaling Technology, USA), rabbit anti-phospho–NF–κB p65 (1:1000, Cell Signaling Technology, USA), rabbit anti-inducible nitric oxide synthase (iNOS) (1:1000, Affinity Biosciences, China), rabbit anti-CD86 (1:1000, Abcam, USA) and rabbit anti-GAPDH (1:1000, Cell Signaling Technology, USA). After washing, the membranes were incubated with the appropriate horseradish peroxidase-conjugated secondary antibodies for 1 h. Bands were visualized using an electrochemical luminescence reagent and the ChemiDoc XRS imaging system (Bio-Rad, USA).

2.16. Immunofluorescence staining

Cells were fixed in 4% formalin solution for 30 min and blocked with 5% bovine serum in 1 × PBS at 4 °C for 3 min. The primary antibodies rabbit anti-CD86 (1:200, Abcam, USA), rabbit anti-iNOS (1:200, Abcam, USA), rabbit anti–NF–κB p65 (1:200, Cell Signaling Technology, USA) and rabbit anti-phospho–NF–κB p65 (1:200, Cell Signaling Technology, USA) were applied to samples at 4 °C overnight and washed off thereafter. The samples were incubated with secondary antibodies (1:1000, Alexa Fluor 488 goat, Beyotime, USA) and FITC-phalloidin at 37 °C for 2 h. The cells were counterstained with DAPI and washed before imaging under an upright microscope.

2.17. Determining the macrophage cytokine secretion profile using ELISA

The relative concentrations of cytokines were quantified (pg/ml) in macrophage culture supernatants after 48 h of stimulation using commercially available ELISA kits. Besides, wound beds and dorsal skin surrounding the wound were incised and cut into pieces in 600 μL PBS solution. The pieces and the solution were transferred in centrifuge tubes and centrifuged at 300 g for 5 min. The supernatants were collected and kept at −80 °C until further analysis. ELISAs for rat tumour necrosis factor-α (TNF-α), interleukin (IL)-10 (ELISA Development System, R&D Systems, Minneapolis, USA) and rat transforming growth factor-β1 (TGF-β1) (ELISA Development System, R&D Systems, USA) were performed according to the manufacturer's instructions.

2.18. Cell scratch assay

A suspension of BMDMs with 400 μg/ml AGEs were cultured on the membranes for 48 h. The same concentration of BMDMs with 400 μg/ml AGEs were cultured in a tissue culture dish as a control. Two collected medium samples were centrifuged at 12,000 rpm for 15 min to remove cell debris and particles, subsequently sterilized by a 0.22 μm filter, and stored at −80 °C before use. Fibroblasts were cultured on plated at 10^4 cells/cm^2. After reaching confluence, the conditioned medium samples and DMEM at 1:1 ratio were added to fibroblasts for 5, 12, 24, and 48 h, respectively. Then, a scratch was made on the cell monolayer using a pipette tip to create an artificial *in vitro* wound.

2.19. Transcriptome sequencing and data analysis

High-throughput sequencing and the subsequent bioinformatics analysis were performed by Lianchuan Biotech (Hangzhou, China). Briefly, a suspension of BMDMs with 400 μg/ml AGEs was cultured on Ag-PCL/GelMA in a six-well plate for 48 h. BMDMs were cultured in a tissue culture dish as a control. Two collected medium samples were centrifuged at 12,000 rpm for 15 min to remove cell debris and particles, subsequently sterilized by a 0.22 μm filter, and stored at −80 °C before use. Fibroblasts were cultured in six-well plates. After allowing the cells to adhere overnight, the fibroblasts were treated with the two types of supernatants for 24 h. Then, the fibroblasts were lysed with TRIzol, and the lysates were stored at −80 °C before sequencing. The amount and purity of RNA in each sample were assessed using a NanoDrop ND-1000 spectrophotometer (NanoDrop Technologies, USA). RNA integrity was determined with an Bioanalyzer 2100 instrument (Agilent Technologies, USA) with RIN number >7.0 and confirmed via denatured agarose gel electrophoresis. Poly(A) RNA was purified from 1 μg of total RNA using Dynabeads Oligo (dT)25–61005 (Thermo Fisher) and two rounds of purification. The poly(A) RNA was fragmented into small pieces using a Magnesium RNA Fragmentation module (cat. E 6150, NEB, USA) at 94 °C for 5–7 min. Then, the cleaved RNA fragments were reverse-transcribed to create cDNA with SuperScript™ II Reverse Transcriptase (cat. 1,896,649, Invitrogen), which was used to synthesize U-labelled second-stranded DNAs with *E. coli* DNA polymerase I (cat. m0209, NEB), RNase H (cat. m0297, NEB) and dUTP solution (cat. R0133, Thermo Fisher). An A-base was added to the blunt ends of each strand to prepare them for ligation to indexed adapters. Each adapter contained a T-base overhang to ligate the adapter to A-tailed fragmented DNA. Single- or dual-indexed adapters were ligated to the fragments, and those with sizes of interest were selected with AMPureXP beads. After heat-labile UDG enzyme (cat.m0280, NEB) treatment of the U-labelled second-stranded DNAs, the ligated products were amplified using PCR under the following conditions: initial denaturation at 95 °C for 3 min; eight cycles of denaturation at 98 °C for 15 s, annealing at 60 °C for 15 s and extension at 72 °C for 30 s; and a final extension at 72 °C for 5 min. The average insert size for the final cDNA library was 300 ± 50 bp. We performed 2 × 150 bp paired-end sequencing (PE150) on an Illumina Novaseq™ 6000 instrument (LC-Bio Technology CO., Ltd., Hangzhou, China) following the manufacturer's recommended protocol.

2.20. Preparing rats for an in vivo wound healing assay

All animal experiments were performed with the approval of the Animal Ethics Committee of the Second Affiliated Hospital of Zhejiang University College of Medicine. All experiments were conducted in accordance with the principles and procedures outlined in the Guide for the Care and Use of Laboratory Animals of the National Institute of Health. Male SD rats (age 8 weeks, weight 190–220 g) were procured from the Experimental Animal Center of Zhejiang University and housed at 22 ± 2 °C under 60% humidity and a 12:12-h light-dark cycle with free access to food and water. The animals were acclimated to the environment for 7 days before initiating the experiments. After 18 h of fasting, the rats were injected intraperitoneally with a single dose (55 mg/kg) of streptozotocin (STZ) dissolved in 0.1 M cold citrate buffer (pH 4.5) to induce hyperglycaemia. The nondiabetic control rats received an equivalent volume of citrate buffer only. Rats with blood glucose levels ≥16.65 mmol/L 1 week later and apparent features of polydipsia, polyphagia and polyuria were considered diabetic. To ensure that all treated animals were diabetic, the experiment began at 2 weeks after STZ was

administered. Blood samples were collected from the caudal vein and analyzed for plasma glucose using a portable blood glucometer (Yuwell, China). Body weights, water intake and food intake were monitored daily.

2.21. Wound healing measurements in diabetic rats

The dorsal hairs of each rat were shaved under anaesthesia (pentobarbital sodium, 30 mg/kg body weight), and the dorsal surface was sterilized with 70% alcohol. Then, a standardized full-thickness 15-mm-diameter wound was created. The wound surface was covered with an Ag-PCL membrane, a PCL/GelMA membrane, an Ag-PCL/GelMA membrane or gauze. The rats were caged individually. Digital photographs of the diabetic wounds were taken on days 0, 5, 10, 15 and 20. The wound size percentage was determined as Au/Ai × 100%, where *Ai* is the initial wound area, and *Au* is the wound area that did not heal. The animals were sacrificed on days 5, 10, 15 and 20 after the operation, and tissue samples were collected and embedded in paraffin. Immunohistochemistry and immunofluorescence staining was performed on 6-μm microtome sections.

2.22. Histological analysis

Haematoxylin and eosin (H&E) staining, Masson's trichrome staining, and Sirius Red staining were performed to assess the pathology and healing of the wounds.

2.23. Immunohistofluorescence and immunohistochemistry

Tissue sections were rehydrated and boiled in sodium citrate buffer for about 20 min for immunofluorescence staining. The primary antibodies rabbit anti-CD86 (1:200, Abcam, USA), rabbit anti-iNOS (1:200, Abcam, USA), anti-keratin 10 (K10; 1:200, Abcam, USA), rabbit anti-CD206 (1:800, Abcam, USA) and mouse anti-CD68 (1:1000, Abcam, USA) were incubated with samples at 4 °C overnight followed by washing. Sections were incubated with secondary antibodies for 2 h at room temperature. DAPI was used to stain nuclei. The sections for immunohistochemical staining were subjected to epitope retrieval in sodium citrate solution. After washing in PBS, the sections were incubated with rabbit anti-AGEs (1:200, Abcam, USA) as a primary antibody overnight at 4 °C. Images were evaluated using an upright microscope.

2.24. Statistical analysis

The data were processed using the statistical software SPSS 25.0 and the measurement data obeyed the normal distribution and were expressed as the mean ± standard deviation. A *t*-test was used for comparison between two groups at the same time point. One-way ANOVA was performed to compare the differences between multiple groups at the same point and two-way ANOVA for comparison between multiple groups at multiple time points. The statistical significance level was set at $p < 0.05$. In the figures, we used * to denote p-values, in which $*p < 0.05$ and $**p < 0.01$.

3. Results

3.1. Physicochemical and surface characterization of the fibrous membranes and morphological changes in macrophages

We fabricated micro/nanofibre membranes using electrospinning technology. Ag-PCL fibrous membranes with different layers of GelMA coating (Ag-PCL, monolayer, bilayer and trilayer) were prepared and characterized to optimize the components used for diabetic wound healing. The surface topography of the different samples as observed using SEM are shown in Fig. 1A. All four electrospun fibres exhibited highly interconnected porosity and a randomly oriented filamentous three-dimensional architecture. Morphological changes in macrophages cultured on different membrane groups as observed using SEM are shown in Fig. 1B. The BMDMs in the Ag-PCL and monolayer groups had a round, pancake-like morphology, whereas those in the bilayer and trilayer groups were elongated in shape (Fig. 1B). The diameter distribution of the fibres is shown in Fig. 1C, revealing an increasing trend in the mean diameter across the Ag-PCL, monolayer, bilayer and trilayer groups. Quantitative results for the spreading area and elongation factor of the cells based on SEM images are shown in Fig. 1D and E, respectively. There was a significantly higher proportion of elongated BMDMs in the bilayer and trilayer groups compared to the Ag-PCL and monolayer groups (Fig. 1E). However, the BMDMs in all four groups had similar spreading areas (Fig. 1D). As shown in Fig. 1F and G, all samples exhibited improved hydrophilicity compared to the uncoated Ag-PCL surface. The swelling ratios of the Ag-PCL, monolayer, bilayer and trilayer groups are shown in Fig. 1H. The swelling ratio of the trilayer group was significantly higher than those of the others ($p < 0.05$).

Water absorption and retention rates are critical features of high-water absorbent materials. The water absorption and retention rates of samples in deionized water, normal saline and solution A are presented in Fig. 1I and J, respectively. All groups of fibrous membranes possessed good water absorption and water retention properties in the solutions studied. The water absorption and retention rates of the four groups increased when the GelMA layer was added (Fig. 1I, J). The water absorption and retention rates of the trilayer GelMA fibrous membranes were highest among all the samples studied in the same solution (Fig. 1I, J). The wound dressing must provide a suitable pH environment for cell growth during the different stages of wound healing. Hence, all fibrous membrane types were placed on top of moist agar (pH 7.4) to mimic this situation, and pH values at the interface were measured with a pH meter (Fig. 1K). Interestingly, a physiological environment (pH 6.8–7.4) was detected at the interface in all groups for 15 days (Fig. 1L). However, the monolayer, bilayer and trilayer groups exhibited relatively higher pH values than did the Ag-PCL group (Fig. 1L).

The mechanical properties of the developed fibrous membranes were investigated by stress-strain and Young's modulus measurements and tensile strength (Fig. 1M−O). As apparent from Fig. 1M, all GelMA-coating fibrous membranes depicted good mechanical support under elongation (Fig. 1M). The greatest tensile strength was found after coating with three layers of GelMA (Fig. 1N). This enhancement was potentially attributed to the filling of voids between Ag-PCL fibres by GelMA. The trilayer group observed a significantly higher Young's modulus for demonstrating a reinforcing action of the GelMA coating (Fig. 1O).

These results demonstrate that fibrous membranes with a trilayer GelMA structure had better water absorption and retention abilities and an enhanced hydrophilic effect, as well as provided a more favourable local environment for wound healing than did the Ag-PCL, monolayer and bilayer groups.

3.2. Antibacterial performance of the fibrous membranes

The antibacterial activity of the fibrous membrane was evaluated using *Escherichia coli* (*E. coli*, gram-negative bacteria) and *Staphylococcus aureus* (*S. aureus*, gram-positive bacteria), and the results were shown in Figure S1. All groups of fibrous membranes have antibacterial effects (Fig. S1). And there was no significant difference in the antibacterial ratio between the Ag-PCL and trilayer groups (Fig. S1). The results illustrated that GelMA coating layers did not affected the antibacterial activity of fibrous membranes.

3.3. Attachment of fibroblasts onto the fibrous membranes and biocompatibility of the fibrous membranes

Cell adhesion is crucial for governing a variety of cellular functions, including cell growth, migration, differentiation and survival and tissue

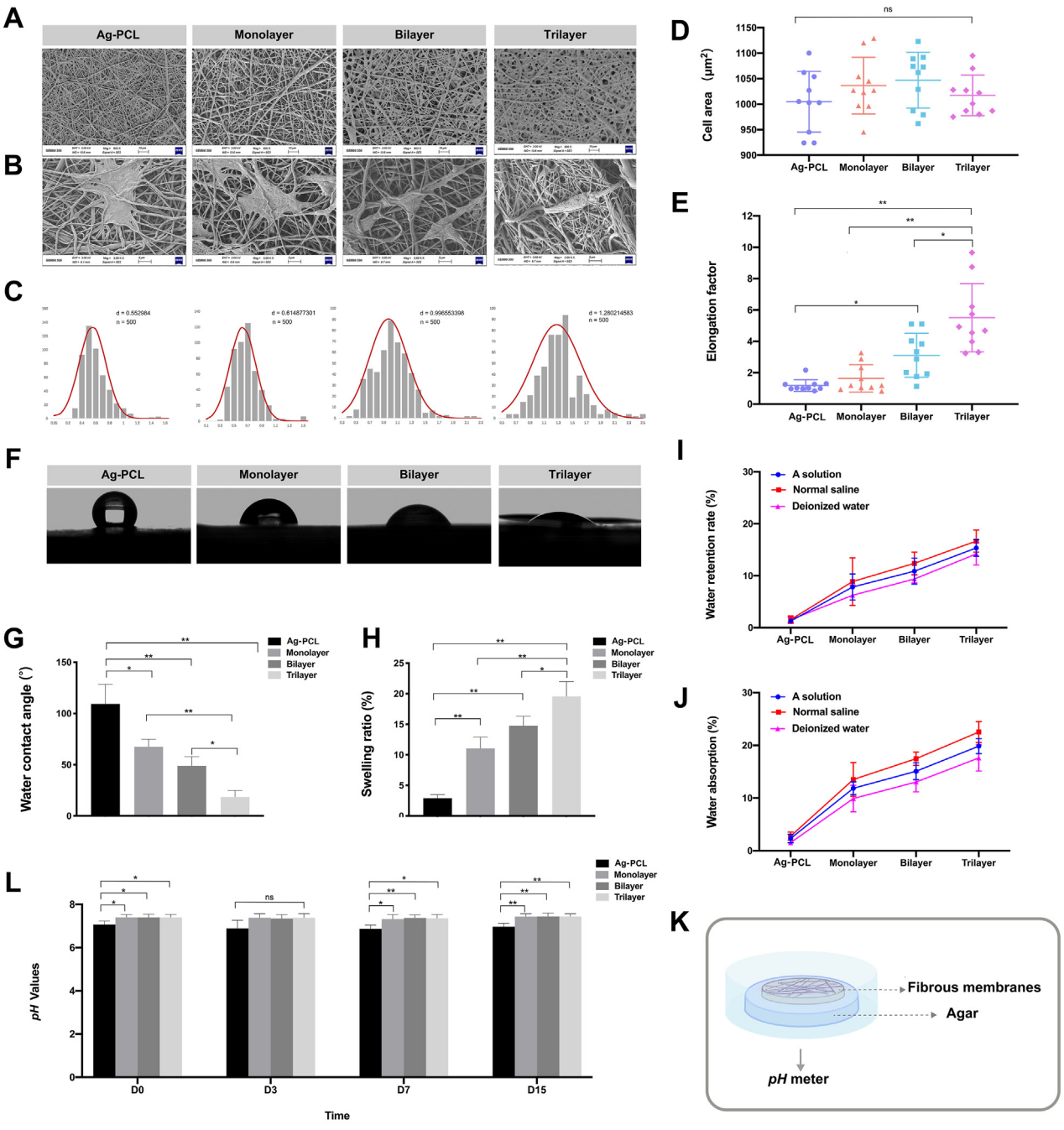

(caption on next page)

Fig. 1. Physicochemical and surface characterizations of fibrous membranes and the morphological changes of macrophages. A) Surface morphologies of different samples under SEM. Scale bars, 10 μm. B) Cell morphologies of macrophages on different samples, Scale bars, 5 μm. C) Diameter distribution of fibrous membranes based on the SEM of surface morphologies. n = 500. D) Quantitative cell area based on SEM images. n = 10. E) Quantification of cell elongation factor based on SEM images. n = 10. F) Digital pictures of water contact angles of different samples. G) Quantification of water contact angles of different samples. n = 3. H) The swelling ratio of different samples. n = 3. I) The water retention rate of different samples. n = 3. J) Water absorption rate of different samples. n = 3. K) Schematic diagram of the method to measure the pH value of substrate surfaces of fibrous membranes. L) Measuring the pH value of substrate surfaces of fibrous membranes on moist agar (pH 7.4) by a Micro-probe pH meter. n = 3. M − O) Mechanical characterizations of the fibrous membranes. n = 3. *P < 0.05 and **P < 0.01.

organization [31]. Hence, we used rat primary fibroblasts to investigate cell attachment in the Ag-PCL, monolayer, bilayer and trilayer groups (Fig. 2). Fibroblasts cultured on Ag-PCL and monolayer membranes for 1 h spread poorly and were round in shape, whereas those on trilayer membranes exhibited a more stellate-patterned morphology (Fig. 2A). The fibroblasts spread rapidly on bilayer and trilayer membranes (Fig. 2A). After 4 h of culture, the fibroblasts in the Ag-PCL and monolayer groups retained a polygon morphology with some protrusions, whereas those cultured on bilayer and trilayer membranes remained long and fusiform, which are morphological features of adherent and spreading fibroblasts (Fig. 2A).

We further used fibroblasts to test the number of live/dead cells to assess the biocompatibility of Ag-PCL, monolayer, bilayer and trilayer membranes *in vitro* (Fig. 2B). The percentage of dead cells increased in the Ag-PCL group, as shown in Fig. 2B and C. However, the cells cultured on trilayer membranes remained alive, and no significant cytotoxic effect was observed. From the results, the proportion of dead cells decreased gradually with an increase in the number of GelMA coating layers. Furthermore, the CCK-8 assay results showed that the cells in the trilayer group were the most viable (Fig. 2D).

Collagen gene expression levels were compared to determine the effect of GelMA immobilization on the expression of fibroblast-specific markers (Fig. 2E). Fibroblasts in the trilayer group expressed the highest level of collagen 1A1 compared to the Ag-PCL, monolayer and bilayer groups after 14 days (Fig. 2E). The cells cultured in the trilayer group exhibited the highest collagen 1A2 expression level for 14 days (Fig. 2E).

The expression levels of fibronectin (FN) and focal adhesion kinase (FAK) were determined after fibroblasts were co-cultured with fibrous membranes for 14 days to further explore the molecular mechanism underlying cell adhesion. Fig. 2E shows that the FAK and FN mRNA levels increased significantly in the bilayer and trilayer groups compared to that in the Ag-PCL group. This tendency was consistent with the results shown

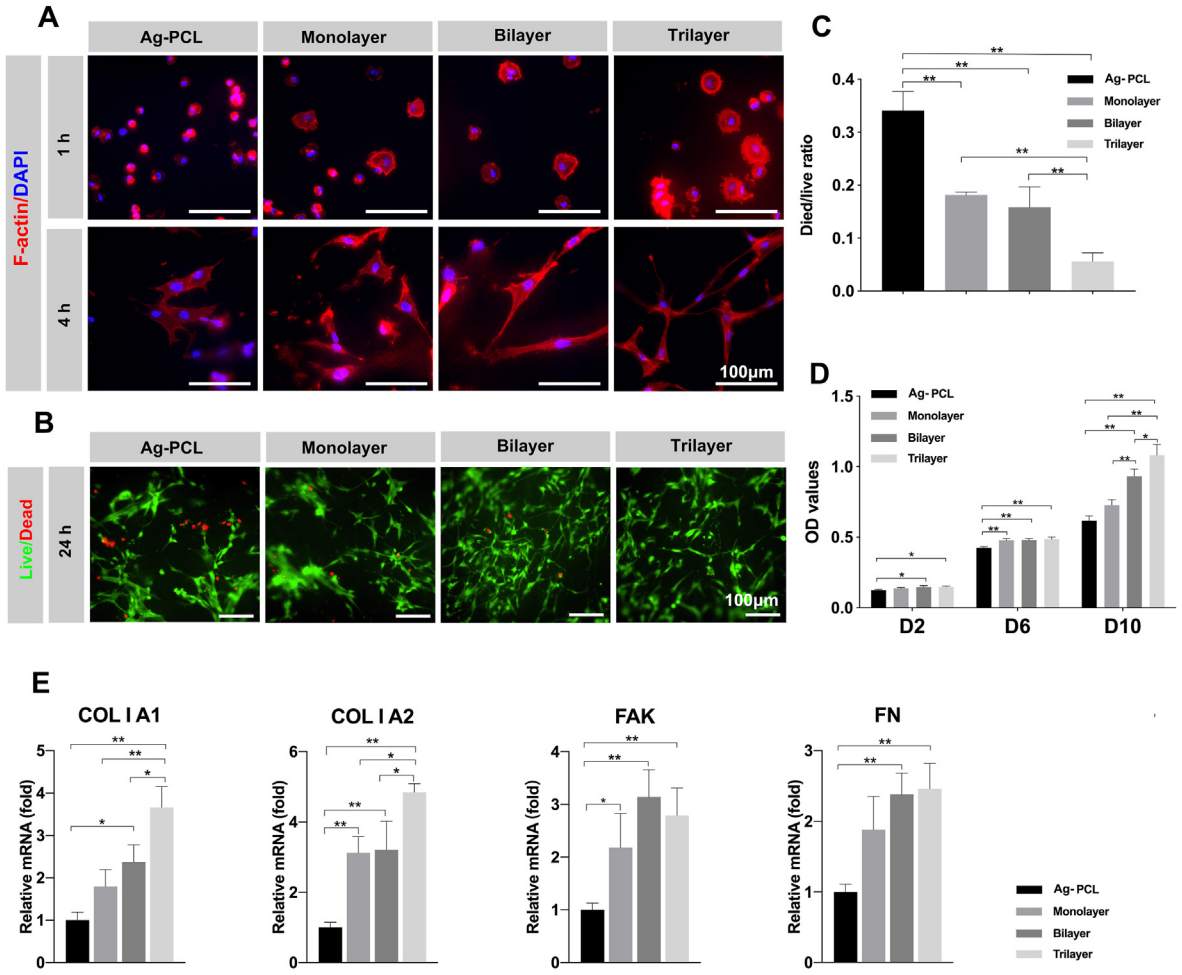

Fig. 2. Attachment of fibroblasts on fibrous membranes and biocompatibility of fibrous membranes A) The adhesion morphology of fibroblasts on the fibrous membranes cultured for 1 and 4 h. Scale bar, 100 μm. B) Live/dead fluorescence images of fibroblasts cultured on different groups of fiber membranes. Scale bar, 100 μm. C) Ratios of number of died cells (red) to live cells (green). D) Cell proliferation was determined as OD value using the CCK-8 assay. E) Gene expression levels of collagen 1A1, collagen 1A2, fibronectin (FN) and focal adhesion kinase (FAK). *P < 0.05, **P < 0.01. (For interpretation of the references to colour/colour in this figure legend, the reader is referred to the Web version of this article.)

in Fig. 2A, confirming better adhesion in the trilayer membrane treatment, which was attributed to the higher expression of adhesion-related proteins and kinases.

Overall, the cell viability and cell attachment studies collectively demonstrated that the trilayer GelMA-coated fibrous membranes improved the attachment, spreading and proliferation of fibroblasts. Therefore, we chose the trilayer GelMA-coated Ag-PCL fibrous membranes (Ag-PCL/GelMA) for subsequent experiments.

3.4. Ag-PCL/GelMA fibrous membranes impair AGE-induced macrophage M1 polarization and promote macrophage M2 polarization

In this experiment, LPS-treated macrophages were taken as the positive control group and untreated macrophages the negative control group. As shown in Fig. 3A, BMDMs flattened into round, pancake-like shapes within 24 h of AGE stimulation. Morphological changes in the macrophages induced by AGEs appeared similar to those induce by LPS stimulation, with both substances inhibiting cell elongation (Fig. 3A). F-actin fluorescence staining was applied to observe the cell ultrastructure of the BMDMs in different groups. Following AGE treatment, the BMDMs exhibited a pancake-like cell morphology, similar to that observed in light microscopy images (Fig. 3B). Interestingly, compared with the BMDMs in the control group, which exhibited a hummingbird-like morphology, the AGE-treated cells bore numerous long, outstretched filopodia (Fig. 3B). These filamentous ultrastructures stretched along the boundary of the BMDMs (Fig. 3B). Similarly, protruding filopodia were found in the LPS-treated group (Fig. 3B). The degree of morphological change was quantified as the length of the longest axis divided by the length of the shortest axis across the cell nucleus (Fig. 3C). As shown in Fig. 3D, AGE-induced macrophages and LPS-induced macrophages exhibited a significantly lower degree of elongation compared to unstimulated M0 cells. The cell spreading area based on F-actin images (Fig. 3B) remained constant across all three macrophage populations (Fig. 3E).

To confirm the macrophage polarization state, immunofluorescent staining and western blotting for iNOS and CD86 were applied to explore whether AGEs induced macrophage M1 polarization. As shown in Fig. 3F, more positive CD86 and iNOS staining were observed in the AGE-treated and LPS-treated groups than in the control group, consistent with the western blotting results (Fig. 3G–H).

The key hypothesis of this study was that the Ag-PCL/GelMA fibrous membranes would modulate AGEs-induced macrophage polarization such that the macrophages would secrete cytokines that contribute to downstream cell activity. To verify this hypothesis, immunofluorescent staining was applied to investigate whether the Ag-PCL/GelMA fibrous membranes induced macrophage polarization. BMDMs were cultured on Ag-PCL/GelMA fibrous membranes and either unstimulated or stimulated with AGEs to polarize the cells towards the M1 pro-inflammatory phenotype. Surface markers with the highest rank-order specificity for M1 (CD86) and M2 (CD206) macrophages were examined in the different groups. iNOS and Arg-1 expression levels in the cytoplasm were considered markers of M1 and M2 macrophage activation. Fig. 3I–L shows the immunofluorescent stained images and the quantitative fluorescence intensity of each macrophage phenotype under different conditions. The presence of Ag-PCL/GelMA effectively reduced the percentage of cells expressing CD86 under AGE stimulation, compared to the control group (Fig. 3I). In the absence of AGEs, Ag-PCL/GelMA did not increase iNOS cell expression, as the two groups had similarly low percentages of iNOS-positive cells (Fig. 3K). After AGE treatment, a decreasing trend in the semi-quantified fluorescence intensity of iNOS was found in the Ag-PCL/GelMA group, compared to the control group (Fig. 3K). Additionally, regardless of the presence or absence of AGEs, the expression of M2 macrophage markers (CD206 and Arg-1) increased significantly in the Ag-PCL/GelMA treatment group (Fig. 3J, L).

Cytokine secretion profiles were assessed using ELISA to explore the functional consequences of fibrous membranes on M0 and AGE-stimulated macrophages (Fig. 3M−P). The results illustrated good concordance with the outcomes mentioned above. Interestingly, under stimulation by AGEs, the secretion levels of the cytokines IL-10 and TGF-β were significantly up-regulated in Ag-PCL/GelMA-treated BMDMs, compared to the control (Fig. 3M, N). As expected, Ag-PCL/GelMA impaired the increase in IL-6 and TNF-α secretion in response to AGE stimulation, and BMDMs in the Ag-PCL/GelMA group secreted significantly less cytokines compared with the cells cultured under control conditions (Fig. 3O, P). Ag-PCL/GelMA had no significant effect on the secretion levels of TNF-α without AGE treatment (Fig. 3P). Overall, macrophages on the Ag-PCL/GelMA membranes secreted less pro-inflammatory cytokines (TNF-α and IL-6) but higher amounts of anti-inflammatory cytokines (TGF-β and IL-10) under AGE stimulation.

3.5. The conditioned medium from Ag-PCL/GelMA-stimulated macrophages reduces inflammation and enhances cell migration in vitro

During the wound healing process, macrophage-fibroblast interactions coordinate tissue repair, and the behaviour of fibroblasts strongly depends on the macrophage phenotype. Here, we analyzed the response of primary rat fibroblasts stimulated with BMDM-released factors in different groups. We focused on the NF-κB pathway as a proxy for "pro-inflammatory activation" since an increase in NF-κB signaling has been related to impaired tissue healing [32]. As shown in Fig. 4A, fibroblasts were co-cultured with conditioned medium from Ag-PCL/GelMA-stimulated macrophages, and nuclear translocation of NF-κB-p65 was analyzed in the fibroblasts at 24 h after stimulation by the conditioned medium. The factors secreted by Ag-PCL/GelMA-stimulated macrophages provoked a significant decrease in p65 nuclear translocation in the fibroblasts compared to exposure to the supernatant of non-Ag-PCL/GelMA-stimulated macrophages (Fig. 4B). Similarly, the western blotting results supported the marked suppression of p65 phosphorylation and nuclear translocation by Ag-PCL/GelMA-stimulated macrophages (Fig. 4C).

To further investigate the effect of regulating macrophages on the behaviours of the major players that participate in wound healing, fibroblasts were co-cultured with Ag-PCL/GelMA-stimulated macrophage-conditioned medium (MCM) and cell migration was assessed. Fibroblasts treated with Ag-PCL/GelMA-stimulated MCM for 24 h exhibited the fastest closure compared to the control MCM-treated cells (Fig. 4D, E).

Collectively, these data indicate that some paracrine factors secreted by Ag-PCL/GelMA-stimulated macrophages inhibited AGE-induced activation of the NF-κB-p65 signaling pathway and significantly enhanced cell migration, implying that Ag-PCL/GelMA possesses the potential to promote wound healing.

3.6. Bioinformatics analysis of fibroblast gene expression

Transcriptomic analysis of fibroblasts cultured in different MCMs was applied to understand how Ag-PCL/GelMA-stimulated MCM enhances cell migration. Fig. 5A shows the many differences in gene expression between Ag-PCL/GelMA-stimulated MCM-treated fibroblasts and control MCM-treated fibroblasts. The differentially expressed genes were collated to perform a Gene Ontology (GO) database analysis. All differentially expressed genes were divided into three classes: cellular components, biological processes and molecular functions (Fig. 5B). The top 20 enriched terms for Ag-PCL/GelMA-stimulated MCM vs. control MCM are shown in Fig. 5C. Of these, myosin II head/neck binding, negative regulation of T cell polarity and negative regulation of protein localization to the cell leading edge were the most enriched. We also performed Kyoto Encyclopaedia of Genes and Genomes (KEGG) analysis of these differentially expressed genes to elucidate the underlying signaling pathways (Fig. 5D). The experimental results in Fig. 4C and D shows that the Ag-PCL/GelMA-stimulated MCM accelerated fibroblast migration. Therefore, we focused on differences in Ag-PCL/GelMA MCM-induced

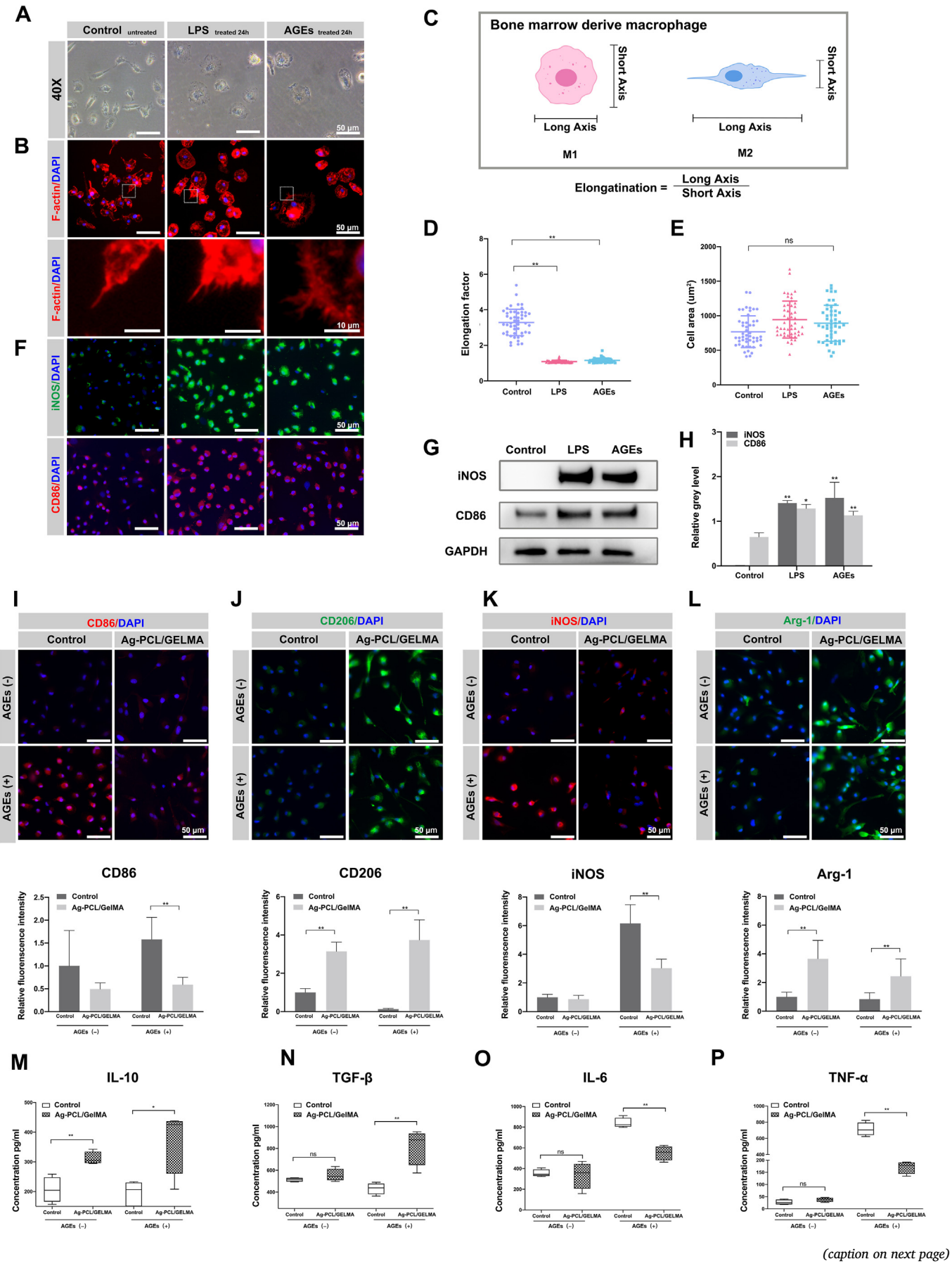

(caption on next page)

Fig. 3. Ag-PCL/GelMA fibrous membranes impair AGEs-induced macrophages M1 polarization and increased macrophages M2 polarization A) The images of BMDMs left untreated (Left) or treated with LPS (Center) or AGEs (Right). Scale bar, 50 μm. B) Fluorescence images of phalloidin-labelled BMDMs. Scale bar, 50 μm (first panel); 10 μm (second panel). C) Scheme of cell morphology change and definition of cell elongation. D) Quantification of elongation, or length of the long axis divided by length of the short axis, for control, LPS-treated, and AGEs-treated cells. n = 50. E) Quantitative cell area based on fluorescence images phalloidin-labelled cells. F) Fluorescence images of BMDMs stained for iNOS (green) and CD 86 (red) and DAPI nuclear counterstain (blue) of control (Left), LPS-treated (Center) and AGEs-treated cells (Right). Scale bar, 50 μm. G) Representative Western blot of iNOS and CD 86 of control, LPS-treated, and AGEs-treated cells. H) The grey levels of iNOS and CD86 were analyzed and normalized to GAPDH. I) Fluorescence images of BMDM stained for CD86 (red) and DAPI nuclear counterstain (blue). And quantitative fluorescence intensity of CD86 of macrophages on different samples. Scale bars, 50 μm. J) Fluorescence images of BMDM stained forCD206 (green) and DAPI nuclear counterstain (blue). And quantitative fluorescence intensity of CD206 of macrophages on different samples. Scale bars, 50 μm. K) Fluorescence images of BMDMs stained for iNOS (red) and DAPI nuclear counterstain (blue). And quantitative fluorescence intensity of iNOS of macrophages on different samples. Scale bars, 50 μm. L) Fluorescence images of BMDMs stained for Arg-1(green) and DAPI nuclear counterstain (blue). And quantitative fluorescence intensity of Arg-1 of macrophages on different samples. Scale bars, 50 μm. M) ELISA analyses of anti-inflammatory cytokines IL-10. N) ELISA analyses of anti-inflammatory cytokines TGF-β. O) ELISA analyses of anti-inflammatory cytokines IL-6. P) ELISA analyses of anti-inflammatory cytokines TNF-α. n = 3. *P < 0.05 and **P < 0.01. (For interpretation of the references to colour/colour in this figure legend, the reader is referred to the Web version of this article.)

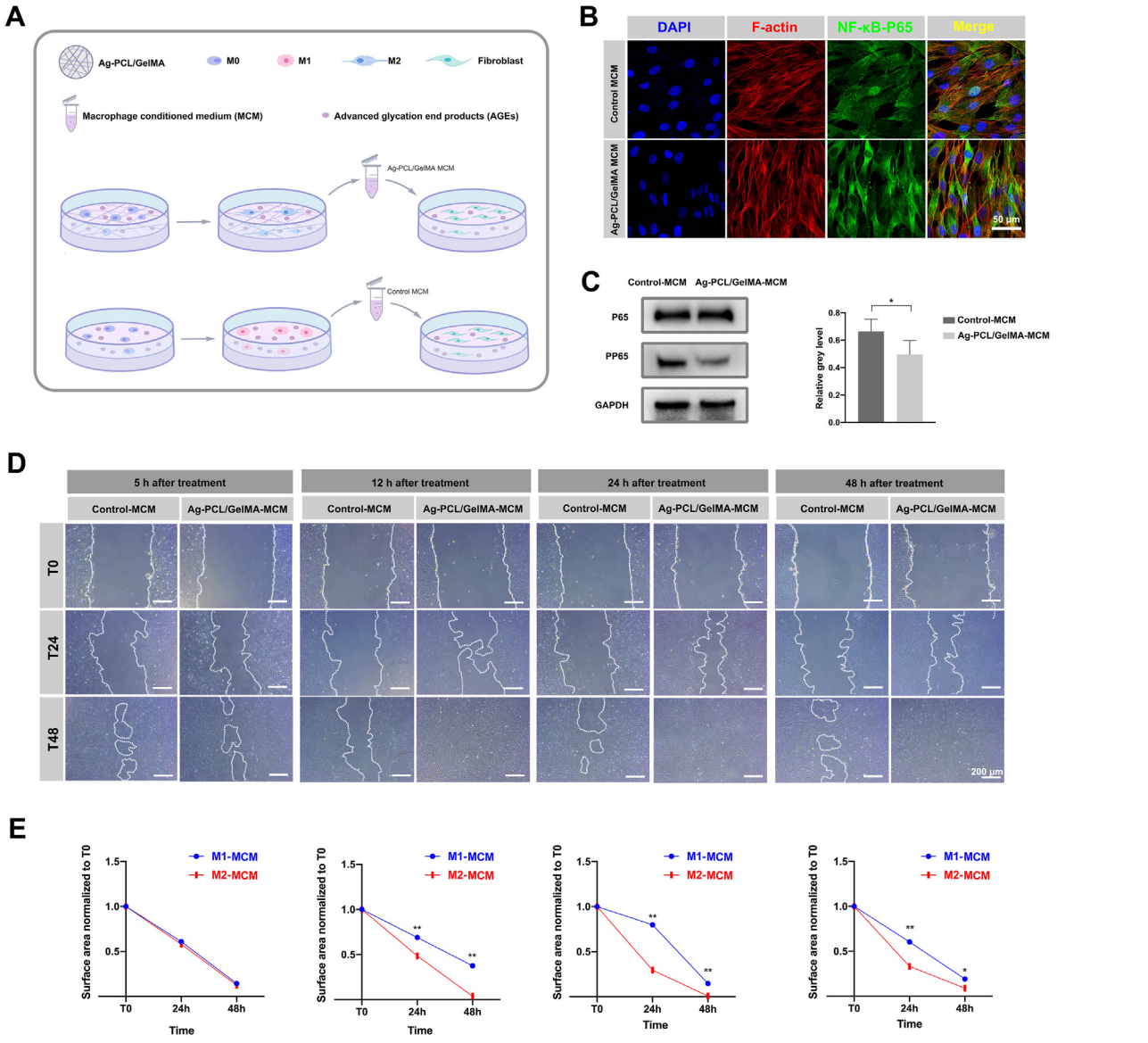

Fig. 4. Ag-PCL/GelMA stimulated macrophage conditioned medium decreases nuclear NF-κB-p65 translocation in fibroblasts and enhanced cell migration in vitro. A) Schematic depicting the process of assessing the nuclear NF-κB-p65 translocation and migration of fibroblasts by different MCMs. (B) Fluorescence images of fibroblasts stimulated with different MCMs stained for F-actin (red), NF-κB-p65 (green) and DAPI (blue), Scale, 50 μm. C) Representative western blot of NF-κB-p65 and phosphorylated NF-κB-p65 (p-p65) in response to MCMs (Left). The grey levels of (p-p65) were quantified and normalized to total protein counterparts (NF-κB-p65) (Right). D) Representative images of MCM-treated fibroblasts in a scratch wound assay. MCMs were applied for different time periods (5, 12, 24 and 48 h). Scale bar, 200 μm. E) The quantification of MCM-treated fibroblasts in a scratch wound assay. n = 4. *$P < 0.05$ and **$P < 0.01$. (For interpretation of the references to colour/colour in this figure legend, the reader is referred to the Web version of this article.)

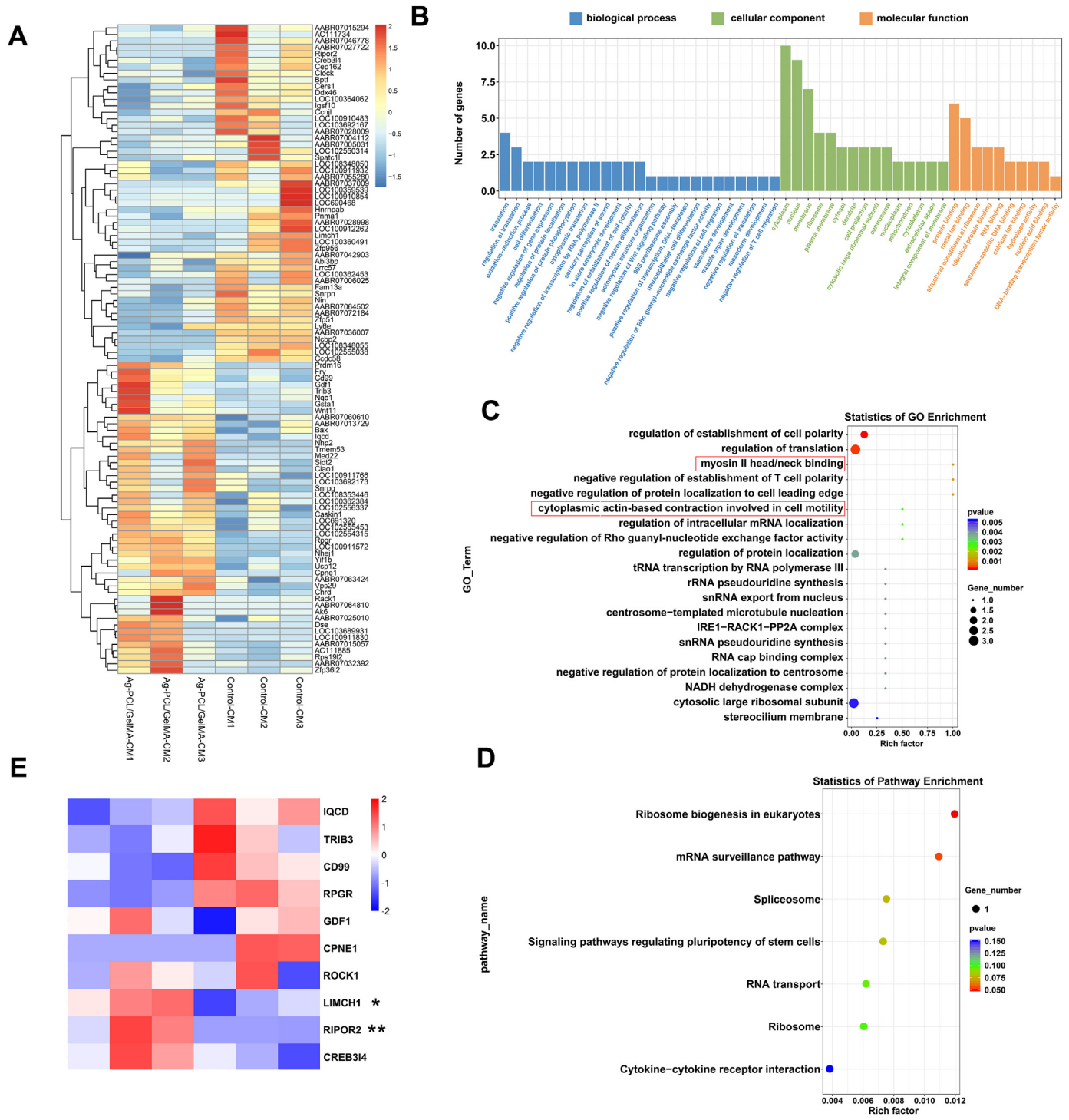

Fig. 5. Bioinformatic analysis of fibroblasts gene expression response to different MCMs and mechanistic analysis of fibroblast migration induced by Ag-PCL/GelMA induced MCMs. A) Transcriptomic analysis of differentially expressed genes. n = 3 independent experiments per group. B, C) GO analysis of all genes in fibroblasts cultured with control-MCM versus Ag-PCL/GelMA-MCM. D) KEGG analysis demonstrating the top 20 signal pathways enriched by differentially expressed genes. E) Heatmap analysis of differentially expressed genes involved in cell migration and cytoskeleton arrangement.

gene expression, including the expression of cell adhesion, migration, cytoskeletal contraction and NF-κB pathway genes. These differentially expressed genes are shown in a heat map (Fig. 5E). In fibroblasts treated with Ag-PCL/GelMA MCM, the expression of RIPOR2 and Limch1 was significantly down-regulated (Fig. 5E).

3.7. Diabetic wound healing in vivo

Based on the result that Ag-PCL/GelMA-induced macrophages impaired polarization of the AGE-stimulated M1 phenotype, increased polarization of the M2 phenotype, and regulated fibroblast behaviour, a

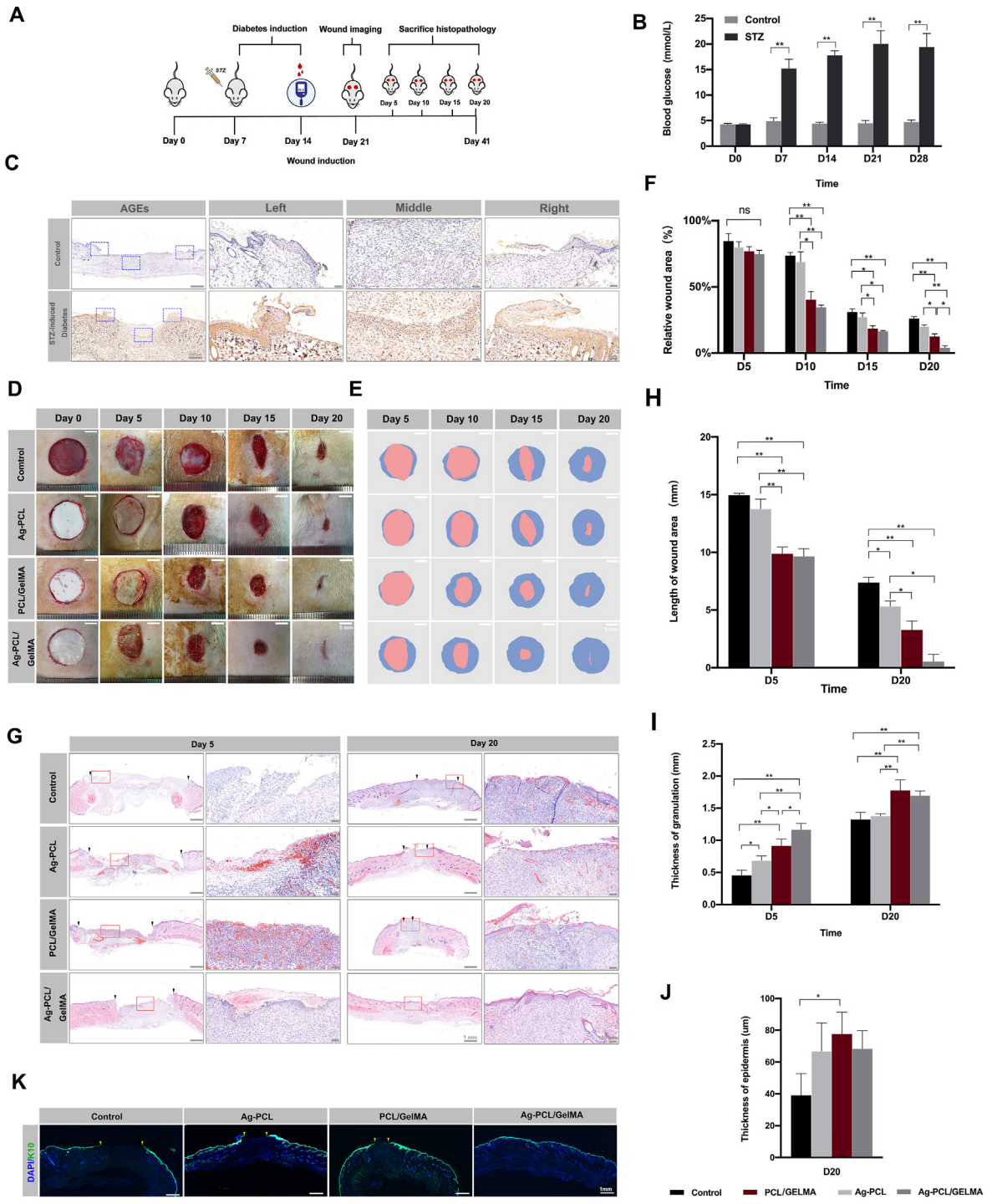

Fig. 6. In vivo diabetic wound healing assay. A) Schematic diagram of the *in vivo* wound healing research on STZ-induced rats. B) Blood glucose levels in STZ-induced rats versus normal rats. C) Representative immunohistochemistry for AGEs in normal rat and STZ-induced rat skin tissue. Scale bar, 500 μm and 50 μm. D) Representative images of wounds in all groups during healing. Scale bar, 5 mm. E) Schematic diagram of wound samples. F) Quantification of relative wound area to day 0 of the four groups at different time points. G) Representative H&E staining images of wound samples from different groups on days 5 and 20. Scale bar, 1 mm and 100 μm. H-J) Quantification of the length, granulation tissue thickness, and epidermis thickness of wounds. K) Representative immunofluorescence staining showed the expression and position of K10 in the skin on day 20 after wounding. Scale bar, 1 mm n = 3 $^{*}P < 0.05$, $^{**}P < 0.01$.

full-thickness skin wound model was established to investigate whether the *in vitro* properties could promote diabetic wound healing. Diabetes was induced in rats with an STZ injection. Rats in the control groups were injected with the same volume of buffer (Fig. 6A). The blood glucose values in the STZ-induced rats were >16.7 mmol/L for 14 days after the STZ injection, indicating successful induction of diabetes. We also investigated the accumulation of AGEs in the skin of STZ-induced rats (Fig. 6B). As shown in Fig. 6C, AGE staining was noted in dermal fibroblasts, the epidermal cell ECM and the endothelial cells of vessels in the STZ-induced rats. Weak staining of AGEs was detected in the wounds of normal rats.

Images were acquired with a digital camera (Fig. 6D) and simulation diagrams prepared (Fig. 6E) for the wounds in each group at four time points, followed by quantitative data analysis (Fig. 6F). During the early

healing stage on day 5, the wound repair progress and relative wound area in the control, Ag-PCL, PCL/GelMA and Ag-PCL/GelMA groups were not significantly different (Fig. 6F). On day 10, the diabetic wounds treated with PCL/GelMA and Ag-PCL/GelMA fibrous membranes were healing significantly faster than those in the control and Ag-PCL groups, but the relative wound area was not different in the PCL/GelMA and Ag-PCL/GelMA groups (Fig. 6F). These results showed that the Ag-PCL/GelMA membranes were more beneficial for the healing of diabetic wounds, compared to fibrous membranes without a GelMA coating. The PCL/GelMA and Ag-PCL/GelMA groups maintained faster wound repair and a smaller relative wound area on day 15 compared to the control and Ag-PCL groups (Fig. 6F). The Ag-PCL/GelMA group exhibited faster

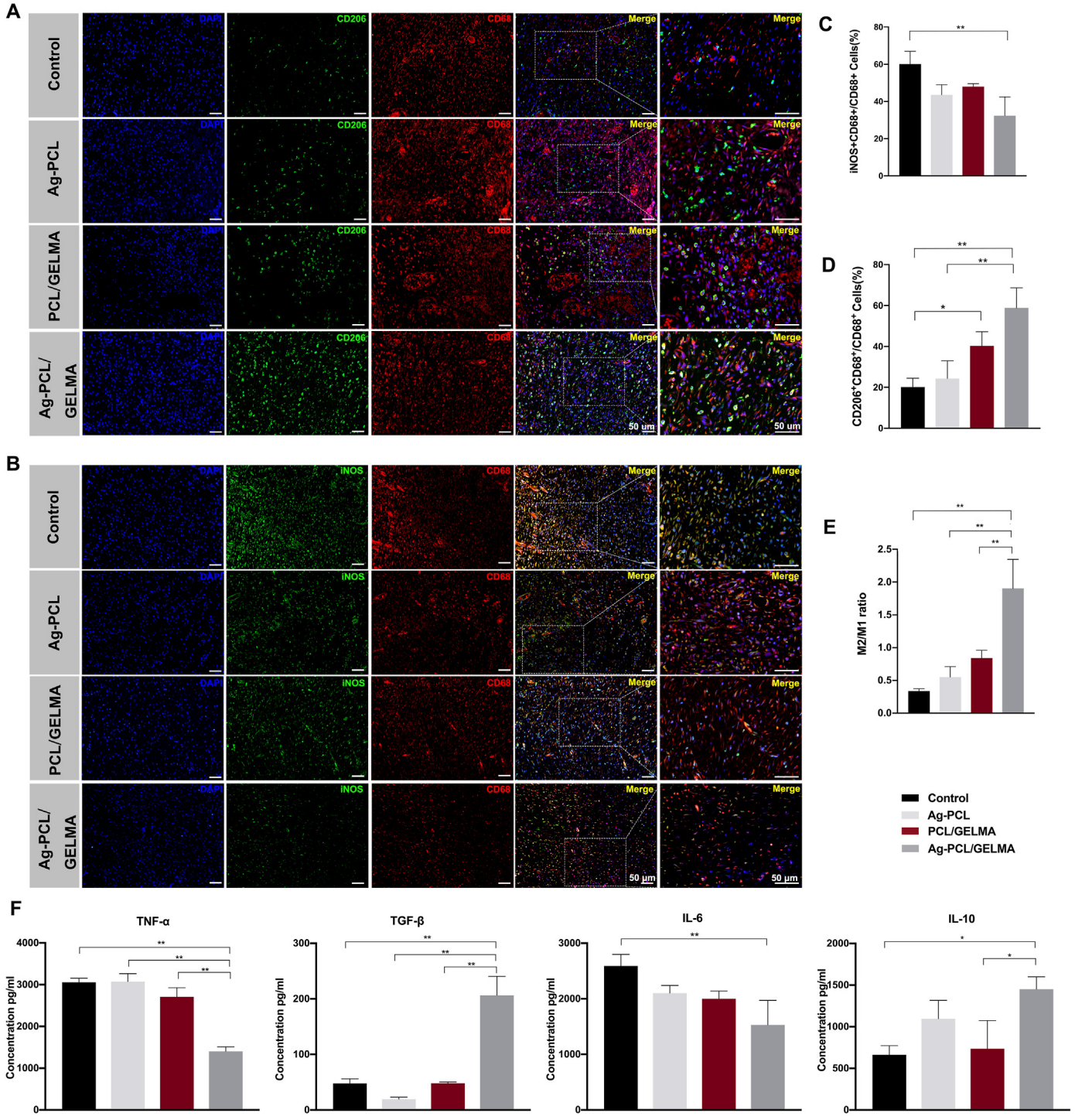

Fig. 7. Ag-PCL/GelMA fibrous membranes relieved inflammation and stimulated M2 polarization of macrophages in diabetic wounds. iNOS+(green, an M1 macrophage marker); CD206+(green, an M2 macrophage marker); and CD68+(red, pan-macrophage marker). A) Representative images of costaining of CD68+and CD206+on day 20. Scale, 50 μm. B) Representative images of costaining of CD68+and iNOS$^+$ on day 20. Scale, 50 μm. C, D) Ratios of number of iNOS (M1-like) or CD206 (M2-like)-positive macrophages to CD68$^+$ macrophages. E) Ratios of number of CD206$^+$ (M2-like) to iNOS$^+$ (M1-like) macrophages in the different groups. F) ELISA analyses of cytokines TNF-α, TGF-β, IL-6, and IL-10. n = 3. *P < 0.05, **P < 0.01. (For interpretation of the references to colour/colour in this figure legend, the reader is referred to the Web version of this article.)

wound repair on day 20, at which time the wounds had almost healed and were covered with neo-epithelium, but the other three groups still had open wounds and eschars (Fig. 6D–F). A smaller relative wound area was observed in the Ag-PCL/GelMA group compared to the control, Ag-PCL and PCL/GelMA groups, indicating the importance of Ag-NPs in the wound healing process (Fig. 6D–F).

H&E staining of wound samples from the different groups was carried out to evaluate the healing and regeneration process on days 5 and 20 (Fig. 6G). The results of statistical analysis of the length of the wound area, thickness of the epidermis and thickness of granulation tissue for the diabetic wounds are shown in Fig. 6H–J, respectively. The length of the wound area shortened and the thickness of granulation tissue increased from days 5–20 in all groups. The Ag-PCL/GelMA group had the shortest wound length ($p < 0.05$) among the groups (Fig. 6H). Abundant newly formed granulation tissue was observed in the Ag-PCL/GelMA and PCL/GelMA groups on day 5, whereas only a small amount of regenerated tissue was seen in samples from the control and Ag-PCL groups. The Ag-PCL/GelMA and PCL/GelMA groups produced significantly more favourable results than the other groups, consistent with the quantitative analysis of the length of the wound area on day 5, although the difference between the Ag-PCL/GelMA and PCL/GelMA groups was not significant (Fig. 6G, H). Wounds with minimal scars in the Ag-PCL/GelMA group were completely covered by neo-epithelium on day 20, whereas those in the other groups still exhibited large defects. Granulation tissue, which was thicker in the wounds treated with Ag-PCL/GelMA and PCL/GelMA compared to the other groups, had a more complex structure with more proliferative fibroblasts on day 20 (Fig. 6G). Moreover, wounds in the Ag-PCL/GelMA, PCL/GelMA and Ag-PCL groups were covered by skin with similar epidermal thicknesses (Fig. 6G, J), indicating that re-epithelialization of these wounds was almost completed. As K10 is an early marker of cell differentiation in the epithelial cell lineage, we also investigated whether K10 increased significantly during re-epithelialization in response to PCL/GelMA or Ag-PCL/GelMA treatment (Fig. 6K).

Taken together, these results illustrate that the healing process was accelerated with a short healing time, abundant granulation tissue formation and less scar tissue in diabetic wounds after Ag-PCL/GelMA fibrous membrane treatment.

3.8. Ag-PCL/GelMA fibrous membranes reduce M1 polarization of macrophages and increase M2 polarization of macrophages in vivo

To detect whether the anti-inflammatory effect of the Ag-PCL/GelMA fibrous membranes was related to the change in macrophage phenotype, we further evaluated diabetic full-thickness wounds. Double-labelling immunofluorescence staining experiments examining iNOS (an M1 marker), CD206 (an M2 marker) and CD68 (a pan-macrophage marker) were performed to identify the macrophage phenotypes within the defect area at 20 days after the surgical operation, and the results are shown in Fig. 7A–E. Overall, the expression of iNOS in Ag-PCL/GelMA group was lower than that in the control group (Fig. 7B, C). In addition, CD206 expression in the Ag-PCL/GelMA group was much higher than in the other groups (Fig. 7A). The proportion of M2 macrophages ($CD206^{+}CD68^{+}$) in the Ag-PCL/GelMA group increased significantly compared to the control and Ag-PCL groups ($p < 0.05$) (Fig. 7D). And the M2/M1 ratios was highest in the Ag-PCL/GelMA group (Fig. 7E).

Furthermore, we evaluated the levels of representative inflammatory cytokines in the wound to assess inflammatory microenvironments influenced by the macrophage phenotypes. Compared with Control, Ag-PCL, and PCL/GelMA groups, a lower content of IL-6 and TNF-α was observed in Ag-PCL/GelMA group on day 14, while the levels of TGF-β and IL-10 significantly increased (Fig. 7F).

These results demonstrate that the Ag-PCL/GelMA fibrous membranes promoted the conversion of macrophages from the pro-inflammatory M1 phenotype to the anti-inflammatory M2 phenotype and improved the inflammatory microenvironment in diabetic rats.

3.9. Collagen deposition and neovascularization in vivo

We also evaluated the deposition and organization of new collagen fibres and angiogenesis. Collagen deposition was systematically evaluated in each group using Masson's trichome and Sirius Red staining. Masson's trichome staining revealed significant collagen deposition and excellent alignment at the regenerated wound site in the Ag-PCL/GelMA group, indicating the positive effect of Ag-PCL/GelMA treatment on the deposition of ECM and the arrangement of collagen (Fig. 8A). The Sirius Red results showed that the amount of organized (red birefringence) and total collagen was significantly greater in Ag-PCL/GelMA-treated wounds than in control wounds (Fig. 8B–D). Furthermore, blood vessels in each group were systematically evaluated via immunofluorescence. The results showed that the number of blood vessels was significantly higher in the Ag-PCL/GelMA and PCL/GelMA groups than in the control and Ag-PCL groups (Fig. 8E and F). The analysis of the endothelial marker CD31 and α-smooth muscle actin revealed an increase in $CD31^{+}$ vessel formation, indicating the potential of Ag-PCL/GelMA to induce angiogenesis (Fig. 8E and F).

4. Discussion

The high systemic blood glucose concentrations resulting from diabetes lead to non-enzymatic glycation of proteins and the formation of AGEs [3,33]. AGEs enhance macrophage polarization to the M1 phenotype and inhibit the proliferation of fibroblasts, resulting in the formation of a pro-inflammatory environment that hampers angiogenesis and re-epithelialization, leading to a non-healing wound [4,34,35]. Moreover, diabetic non-healing wounds are easily infected by bacteria, which accelerate and aggravate the pathology of the diabetic wound [36]. Improving the AGE-induced microenvironment by impairing macrophage M1 polarization has been a major goal of therapeutic interventions to accelerate diabetic wound healing. Some factors, such as IL-10 and IL-4, have been used to modulate macrophage polarization, but their cost and associated adverse reactions are huge challenges in applications for diabetic wound treatment [37,38]. However, few studies have examined whether AGE-induced macrophage polarization can be regulated by biomaterial design. In this study, we developed a photosensitive Ag-PCL/GelMA fibrous membrane with antibacterial, anti-inflammatory and moisture-retaining properties. The Ag-PCL/GelMA fibrous membranes impaired AGE-stimulated polarization towards the M1 phenotype and promoted macrophage polarization towards the M2 phenotype. The Ag-PCL/GelMA fibrous membranes thus indirectly accelerated the proliferation and migration of fibroblasts *in vitro*. The Ag-PCL/GelMA membranes also effectively accelerated the healing of full-thickness diabetic wounds.

Modifying the surface cues of biomaterials is a powerful tool with which to modulate the phenotype polarization and functions of macrophages without using specific cytokines in the local tissue microenvironment [16]. Surface cues during the early period can override the effects of underlying soluble cues to polarize macrophages following initial cellular contact with biomaterials [39]. Moreover, physical cues have a longer performance time and can be easily well defined [40]. Data on interactions between micro/nanoscale materials and macrophage responses have deepened the basic knowledge on how to design materials with immunomodulatory properties [41]. Alterations of micro/-nanostructures can bring about significant changes in properties, such as topography, fibre diameter, roughness, stiffness and wettability [42]. Macrophages secrete less inflammatory cytokines on fibrous films than on flat films [43]. BMDMs acquire a pro-healing phenotype on scaffolds with larger fibres, as evidenced by the increased production of growth factors [44]. A rough surface activates M2 macrophage polarization, compared with a smooth surface [45]. The hydrophilicity of the surface transforms RAW 264.7 macrophages into the M2 phenotype [46]. In our experiment, we compared the surface properties of different fibrous membranes. Fig. 1 shows that the hydrophilicity of the fibrous

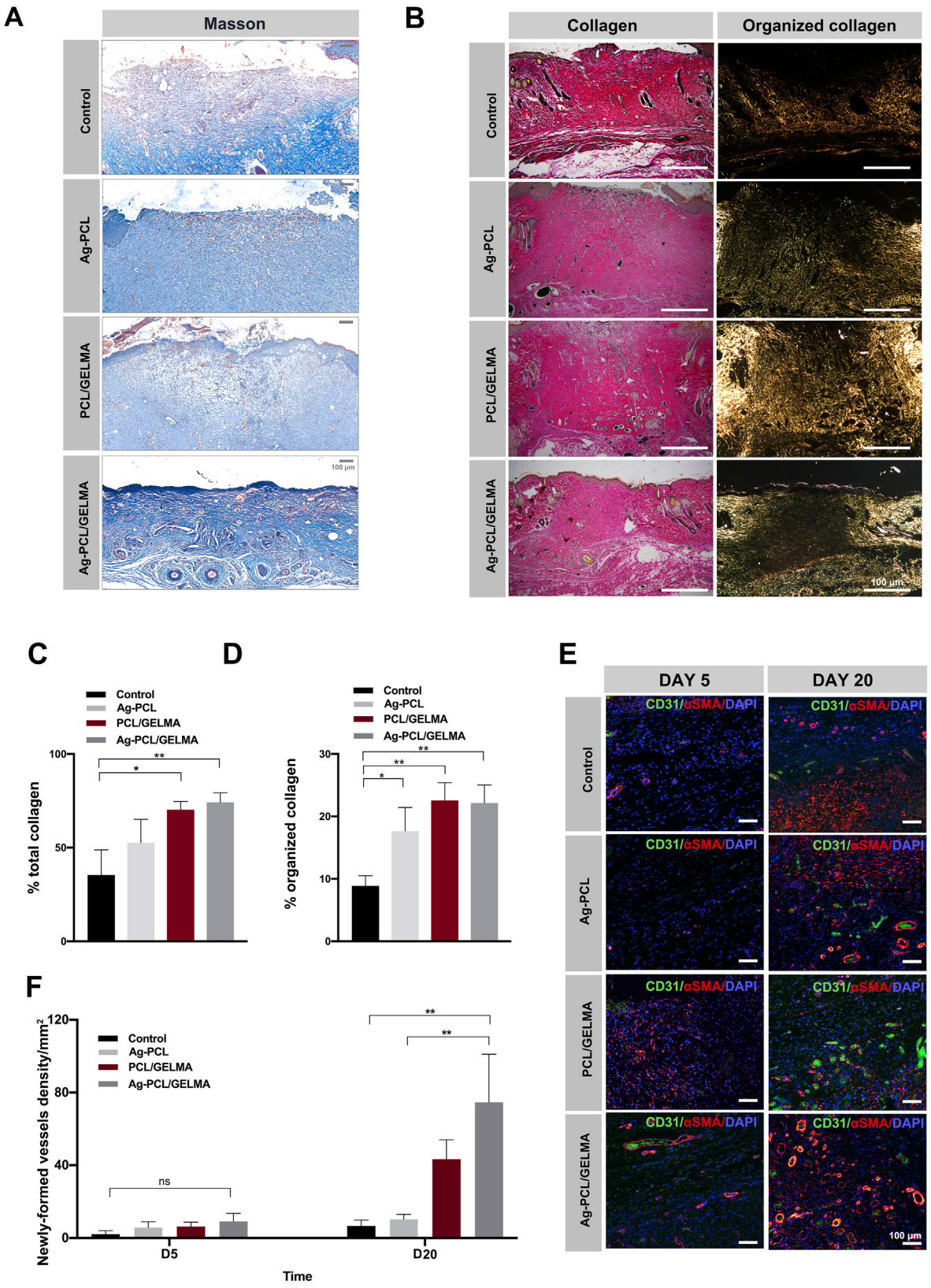

Fig. 8. Ag-PCL/GelMA fibrous membranes enhanced ECM synthesis and vascularization in diabetic wounds. A) Masson's trichrome stained section on day 20 days wounding. Scale bar, 100 μm. B) Representative Sirius Red stained section on day 20 after wounding. Scale bar, 100 μm. C, D) Percentage of total collagen formation and percentage organized collagen on the total collagen was evaluated in different groups. E) Representative immunofluorescence on day 20 after wounding showing presence of $CD31^{+}$ and α-SMA^{+} vessels. Scale bar, 100 μm. F) Quantitative analysis of newly-formed vessels density/mm^{2}. *$P < 0.05$, **$P < 0.01$. (For interpretation of the references to colour/colour in this figure legend, the reader is referred to the Web version of this article.)

membranes was increased, the diameter of the fibres was larger, and the Yang's modulus was improved as the number of GelMA layers increased. In addition, the GelMA coating made the pH value of membranes tend to be neutral, which might be due to the hydrolysis of GelMA (7.4). The pH value around 7.4, providing a more suitable microenvironment for cell proliferation. Under the AGE condition, a trilayer GelMA coating of the fibrous membranes effectively activated cellular elongation, which is the morphology associated with M2 polarization (Fig. 1B). When macrophages approach and/or contact micro/nanostructures, the surface signals of the biomaterials are sensed by the macrophages, which elicits a response from the cells. A previous mechanistic study unveiled that the surface hydrophilicity can activate the PI3K and NF- κB signaling pathways through the selective expression of integrin β1 or β2, thereby driving the macrophage to the M2 phenotype [46]. In addition, for material surfaces with a low Yang's modulus, the nanostructures easily deform, causing stretching of cells adhered to the surface, increasing cell spreading area, and promoting macrophages to polarize into the M1 phenotype to boost inflammation. The molecular mechanism was verified to be related to the FAK–NF–κB signaling pathway [47]. Furthermore, the expression of Arg1 increased while iNOS decreased with increasing fibrous diameter through a mechanism involving multiple TLR/MyD88-dependent pathways [44]. Additionally, surface cues of the material can enhance the anti-inflammatory function of cells that have already been transformed into the M2 phenotype [16]. Therefore, we speculate that changes in surface properties of the fibrous membranes activated and maintained the M2 polarization state of the macrophages.

In our study, the pancake-like cell morphology and high expression of CD86 and iNOS confirmed that the polarization of these macrophages was towards the M1 phenotype. A previous study showed that AGEs induce macrophage polarization towards the M1 phenotype via the hypoxia-inducible factor-1α/PDK4 pathway [4]. In addition, we found that AGE-induced macrophages adapted by rearranging their cytoskeleton and forming filopodia, whereas M0 macrophages adapted a hummingbird-like morphology that hampered the formation of filopodia. The migration of macrophages is closely regulated by cell polarization due to dynamic changes in the cytoskeleton [48], indicating that macrophages become increasingly motile, allowing migration into tissues, whereas M0 macrophages with decreased motility are limited in their ability to migrate.

All of these results strongly suggest the ability of Ag-PCL/GelMA fibrous membranes to promote the polarization of macrophages towards the M2 phenotype *in vitro* (Fig. 3). After macrophages are activated to become M2 macrophages, they secrete pro-healing cytokines and chemokines [49]. In our study, we showed that the Ag-PCL/GelMA membranes enhanced the secretion of some specific chemokines and cytokines from M2 macrophages *in vitro*, including TGF-β and IL-10. TGF-β is a cytokine that functions during wound healing [50,51]. It has been reported to stimulate the proliferation of fibroblasts and ECM synthesis, which support the formation of granulation tissue at the wound site [52]. IL-10 inhibits the release of pro-inflammatory cytokines [53] and has emerged as a key mediator of the pro-inflammatory-to-*anti*-inflammatory transition that counters collagen deposition [54]. In addition, the presence of IL-10 during the later stage of wound healing is correlated with enhanced epithelialization [55]. TGF-β1 and IL-10 regulate the balance between tissue formation and scarring during the tissue repair process [56].

In the present study, Ag-PCL/GelMA membranes directly promoted the proliferation of fibroblasts *in vitro*. Moreover, conditioned medium from Ag-PCL/GelMA-treated macrophages effectively increased the *in vitro* migration of fibroblasts. We presumed that the latter result was mainly due to the increased secretion of cytokines in the MCM that recruit fibroblasts, rather than to the Ag-PCL/GelMA membranes, which directly promoted the migration of fibroblasts. Once endogenous fibroblasts were recruited to the wound site by Ag-PCL/GelMA-activated macrophages, they were further affected by Ag-PCL/GelMA to create a favourable microenvironment in which to synthesize collagen. One study reported that the chemokines and cytokines secreted by macrophages play an important role in recruiting repair cells *in vivo* [57]. Another study reported that the enhancement of wound healing mediated by biomaterials was abolished in the absence of macrophages [58]. Macrophage-fibroblast interactions are responsible for ECM synthesis in the dermis during wound repair [59]. Although this cross-talk is likely to be central to the eventual outcome, the cellular interactions are complex and challenging to study [60]. Other undetected cytokines might have been present in the conditioned medium from Ag-PCL/GelMA-treated macrophages, which might then have a combined effect on cell repair. Therefore, our future studies will focus on investigating the roles of these undetected cytokines.

Cell migration is driven by the cytoskeleton, which mainly comprises actin microfilaments, microtubules and intermediate filaments [61]. The Rho family of small GTPases orchestrates cell migration through multiple effects on the cytoskeleton [62]. The down-regulation of Ripor2 through changes in actin or the microtubule network promotes cell migration. Transcriptomic analysis revealed that calponin homologous domain-containing protein (Limch)-1 was down-regulated in fibroblasts cultured in conditioned medium from Ag-PCL/GelMA nanofibres. LIM and Limch are involved in negatively regulating cell spreading and cell migration [63]. Limch-1 activates the non-muscle myosin IIa complex by promoting the phosphorylation of its regulatory subunit MRLC/MYL9, positively regulates actin stress fibre assembly and stabilizes focal adhesions [63,64]. Cytoskeleton rearrangement-related genes, such as CD99, IQCD and RPGR, were up-regulated. This might have resulted in constant crosstalk between actin, microtubules and intermediate filaments, which would facilitate cell migration [61].

In summary, the multifunctional Ag-PCL/GelMA fibrous membranes showed a remarkable potential for accelerating the healing of diabetic wounds. By effectively impairing AGE-induced M1 polarization and promoting immune-regulation of macrophage polarization towards the M2 phenotype, the Ag-PCL/GelMA fibrous membranes efficiently reduced inflammation, increased neovascularization and enhanced collagen deposition and epithelialization, resulting in relatively satisfactory healing results. Nevertheless, some important questions should be addressed in future work. First, macrophages are thought to exist along a spectrum of phenotypes with two extremes: classically activated macrophages (M1) and alternatively activated macrophages (M2). The *in vivo* status of activated macrophages probably lies on a continuum between these two extreme states. Subsets of macrophages should be accurately regulated by design modifications of biomaterials. Second, a macrophage and fibroblast co-culture system is needed to investigate the interaction between macrophages and fibroblasts, such as whether the macrophage phenotype is altered by fibroblasts.

5. Conclusions

In summary, we developed a bioactive antibacterial, anti-inflammatory, moisturizing fibrous dressing for healing diabetic wounds. The Ag-PCL/GelMA fibrous membranes efficiently impaired AGE-induced macrophage M1 polarization and increased the number of anti-inflammatory M2 macrophages, and their reparative secretions significantly improved the migration of fibroblasts *in vitro* through a paracrine mechanism. *In vivo* experiments demonstrated that the Ag-PCL/GelMA fibrous membranes promoted diabetic wound healing by regulating the inflammatory microenvironment and modulating the activation state of macrophages, subsequently promoting neovascularization and collagen deposition in the wound bed. Taken together, Ag-PCL/GelMA fibres were found to promote diabetic wound healing and exhibit remarkable potential in immunomodulation-related wound therapy.

Funding

This work was financially supported by the National key research and

development project (2016YFC1100800, 2016YFC1100803), the National Natural Science Foundation of China (81772069, 81401591, 8217080154) and Zhejiang Provincial Basic Public Welfare Research Program (LGF19H150008, LGF20H150004).

Contributions

WZ and SX contributed equally to this paper. WZ and SX conceived and designed experiments. TW, MY, ZZ, JS, MZ, JW, PX, JW, RJ, MY, CH conducted the experiments and obtained the results. MZ and MY sorted and analyzed the results; WZ and SX wrote the draft. XW and CH extensively revised, formatted, and submitted versions of the manuscript. All authors participated in data discussions. All authors read and approved the final manuscript.

Data availability

The analyzed data sets generated during the study are available from the corresponding author on reasonable request.

Declaration of competing interest

The authors declare that they have no known competing financial interests or personal relationships that could have appeared to influence the work reported in this paper.

Appendix A. Supplementary data

Supplementary data to this article can be found online at https://doi.org/10.1016/j.mtbio.2022.100395.

References

[1] L.N. Kasiewicz, K.A. Whitehead, Recent advances in biomaterials for the treatment of diabetic foot ulcers, Biomater. Sci. 5 (10) (2017) 1962–1975, https://doi.org/10.1039/c7bm00264e.
[2] N. Ahmed, Advanced glycation endproducts–role in pathology of diabetic complications, Diabetes Res. Clin. Pract. 67 (1) (2005) 3–21, https://doi.org/10.1016/j.diabres.2004.09.004.
[3] H.J. Kang, S. Kumar, A. D'Elia, B. Dash, V. Nanda, H.C. Hsia, M.L. Yarmush, F. Berthiaume, Self-assembled elastin-like polypeptide fusion protein coacervates as competitive inhibitors of advanced glycation end-products enhance diabetic wound healing, J. Contr. Release 333 (2021) 176–187, https://doi.org/10.1016/j.jconrel.2021.03.032.
[4] X. Han, W. Ma, Y. Zhu, X. Sun, N. Liu, Advanced glycation end products enhance macrophage polarization to the M1 phenotype via the HIF-1alpha/PDK4 pathway, Mol. Cell. Endocrinol. 514 (2020), 110878, https://doi.org/10.1016/j.mce.2020.110878.
[5] X. Jin, T. Yao, Z. Zhou, J. Zhu, S. Zhang, W. Hu, C. Shen, Advanced glycation end products enhance macrophages polarization into M1 phenotype through activating RAGE/NF-kappaB pathway, BioMed Res. Int. 2015 (2015), 732450, https://doi.org/10.1155/2015/732450.
[6] R. Klopfleisch, Macrophage reaction against biomaterials in the mouse model - phenotypes, functions and markers, Acta Biomater. 43 (2016) 3–13, https://doi.org/10.1016/j.actbio.2016.07.003.
[7] X. He, L. Dai, L. Ye, X. Sun, O. Enoch, R. Hu, X. Zan, F. Lin, J. Shen, A vehicle-free antimicrobial polymer hybrid gold nanoparticle as synergistically therapeutic platforms for Staphylococcus aureus infected wound healing, Adv. Sci. 9 (14) (2022), e2105223, https://doi.org/10.1002/advs.202105223.
[8] F.M. Davis, A. Kimball, A. Boniakowski, K. Gallagher, Dysfunctional wound healing in diabetic foot ulcers: new crossroads, Curr. Diabetes Rep. 18 (1) (2018) 2, https://doi.org/10.1007/s11892-018-0970-z.
[9] Y. Qian, Y. Zheng, J. Jin, X. Wu, K. Xu, M. Dai, Q. Niu, H. Zheng, X. He, J. Shen, Immunoregulation in diabetic wound repair with a photoenhanced glycyrrhizic acid hydrogel scaffold, Adv. Mater. 34 (29) (2022), e2200521, https://doi.org/10.1002/adma.202200521.
[10] R. Edwards, K.G. Harding, Bacteria and wound healing, Curr. Opin. Infect. Dis. 17 (2) (2004) 91–96, https://doi.org/10.1097/00001432-200404000-00004.
[11] H. Jahan, M.I. Choudhary, Gliclazide alters macrophages polarization state in diabetic atherosclerosis in vitro via blocking AGE-RAGE/TLR4-reactive oxygen species-activated NF-kbeta nexus, Eur. J. Pharmacol. 894 (2021), 173874, https://doi.org/10.1016/j.ejphar.2021.173874.
[12] Z. Zhou, Y. Tang, X. Jin, C. Chen, Y. Lu, L. Liu, C. Shen, Metformin inhibits advanced glycation end products-induced inflammatory response in murine macrophages partly through AMPK activation and RAGE/NFkappaB pathway suppression, J. Diabetes Res. (2016), 4847812, https://doi.org/10.1155/2016/4847812, 2016.
[13] S. Matoori, A. Veves, D.J. Mooney, Advanced bandages for diabetic wound healing, Sci. Transl. Med. 13 (585) (2021), https://doi.org/10.1126/scitranslmed.abe4839.
[14] F.Y. McWhorter, C.T. Davis, W.F. Liu, Physical and mechanical regulation of macrophage phenotype and function, Cell. Mol. Life Sci. 72 (7) (2015) 1303–1316, https://doi.org/10.1007/s00018-014-1796-8.
[15] H. Atcha, A. Jairaman, J.R. Holt, V.S. Meli, R.R. Nagalla, P.K. Veerasubramanian, K.T. Brumm, H.E. Lim, S. Othy, M.D. Cahalan, M.M. Pathak, W.F. Liu, Mechanically activated ion channel Piezo1 modulates macrophage polarization and stiffness sensing, Nat. Commun. 12 (1) (2021) 3256, https://doi.org/10.1038/s41467-021-23482-5.
[16] F.Y. McWhorter, T. Wang, P. Nguyen, T. Chung, W.F. Liu, Modulation of macrophage phenotype by cell shape, Proc. Natl. Acad. Sci. USA 110 (43) (2013) 17253–17258, https://doi.org/10.1073/pnas.1308887110.
[17] Y. Niu, F.J. Stadler, X. Yang, F. Deng, G. Liu, H. Xia, HA-coated collagen nanofibers for urethral regeneration via in situ polarization of M2 macrophages, J. Nanobiotechnol. 19 (1) (2021) 283, https://doi.org/10.1186/s12951-021-01000-5.
[18] C. Yang, C. Zhao, X. Wang, M. Shi, Y. Zhu, L. Jing, C. Wu, J. Chang, Stimulation of osteogenesis and angiogenesis by micro/nano hierarchical hydroxyapatite via macrophage immunomodulation, Nanoscale 11 (38) (2019) 17699–17708, https://doi.org/10.1039/c9nr05730g.
[19] J. Li, X. Jiang, H. Li, M. Gelinsky, Z. Gu, Tailoring materials for modulation of macrophage fate, Adv. Mater. 33 (12) (2021), e2004172, https://doi.org/10.1002/adma.202004172.
[20] R. Augustine, A. Hasan, N.K. Patan, Y.B. Dalvi, R. Varghese, A. Antony, R.N. Unni, N. Sandhyarani, A.A. Moustafa, Cerium oxide nanoparticle incorporated electrospun poly(3-hydroxybutyrate-co-3-hydroxyvalerate) membranes for diabetic wound healing applications, ACS Biomater. Sci. Eng. 6 (1) (2020) 58–70, https://doi.org/10.1021/acsbiomaterials.8b01352.
[21] W. Zhang, T. Weng, Q. Li, R. Jin, C. You, P. Wu, J. Shao, S. Xia, M. Yang, C. Han, X. Wang, Applications of poly(caprolactone)-based nanofibre electrospun scaffolds in tissue engineering and regenerative medicine, Curr. Stem Cell Res. Ther. 16 (4) (2021) 414–442, https://doi.org/10.2174/1574888X15666201014145703.
[22] M.K. Ahmed, M.A. Zayed, S.I. El-Dek, M.A. Hady, D.H. El Sherbiny, V. Uskokovic, Nanofibrous epsilon-polycaprolactone scaffolds containing Ag-doped magnetite nanoparticles: physicochemical characterization and biological testing for wound dressing applications in vitro and in vivo, Bioact. Mater. 6 (7) (2021) 2070–2088, https://doi.org/10.1016/j.bioactmat.2020.12.026.
[23] Y. Yuan, L. Ding, Y. Chen, G. Chen, T. Zhao, Y. Yu, Nano-silver functionalized polysaccharides as a platform for wound dressings: a review, Int. J. Biol. Macromol. 194 (2022) 644–653, https://doi.org/10.1016/j.ijbiomac.2021.11.108.
[24] C. Zhu, R. Cao, Y. Zhang, R. Chen, Metallic ions encapsulated in electrospun nanofiber for antibacterial and angiogenesis function to promote wound repair, Front. Cell Dev. Biol. 9 (2021), 660571, https://doi.org/10.3389/fcell.2021.660571.
[25] A.A. Hassan, H.A. Radwan, S.A. Abdelaal, N.S. Al-Radadi, M.K. Ahmed, K.R. Shoueir, M.A. Hady, Polycaprolactone based electrospun matrices loaded with Ag/hydroxyapatite as wound dressings: morphology, cell adhesion, and antibacterial activity, Int. J. Pharm. 593 (2021), 120143, https://doi.org/10.1016/j.ijpharm.2020.120143.
[26] H. Cheng, Z. Shi, K. Yue, X. Huang, Y. Xu, C. Gao, Z. Yao, Y.S. Zhang, J. Wang, Sprayable hydrogel dressing accelerates wound healing with combined reactive oxygen species-scavenging and antibacterial abilities, Acta Biomater. 124 (2021) 219–232, https://doi.org/10.1016/j.actbio.2021.02.002.
[27] Y. Liu, M.B. Chan-Park, A biomimetic hydrogel based on methacrylated dextran-graft-lysine and gelatin for 3D smooth muscle cell culture, Biomaterials 31 (6) (2010) 1158–1170, https://doi.org/10.1016/j.biomaterials.2009.10.040.
[28] W. Mao, M.K. Kang, J.U. Shin, Y.J. Son, H.S. Kim, H.S. Yoo, Coaxial hydro-nanofibrils for self-assembly of cell sheets producing skin bilayers, ACS Appl. Mater. Interfaces 10 (50) (2018) 43503–43511, https://doi.org/10.1021/acsami.8b17740.
[29] Q.Q. Wang, Y. Liu, C.J. Zhang, C. Zhang, P. Zhu, Alginate/gelatin blended hydrogel fibers cross-linked by Ca(2+) and oxidized starch: preparation and properties, Mater. Sci. Eng. C Mater. Biol. Appl. 99 (2019) 1469–1476, https://doi.org/10.1016/j.msec.2019.02.091.
[30] D. Klose, N. Azaroual, F. Siepmann, G. Vermeersch, J. Siepmann, Towards more realistic in vitro release measurement techniques for biodegradable microparticles, Pharm. Res. (N. Y.) 26 (3) (2009) 691–699, https://doi.org/10.1007/s11095-008-9747-4.
[31] Y. Zhang, L. Hu, D. Yu, C. Gao, Influence of silica particle internalization on adhesion and migration of human dermal fibroblasts, Biomaterials 31 (32) (2010) 8465–8474, https://doi.org/10.1016/j.biomaterials.2010.07.060.
[32] A.C. Abraham, S.A. Shah, M. Golman, L. Song, X. Li, I. Kurtaliaj, M. Akbar, N.L. Millar, Y. Abu-Amer, L.M. Galatz, S. Thomopoulos, Targeting the NF-kappaB signaling pathway in chronic tendon disease, Sci. Transl. Med. 11 (481) (2019), https://doi.org/10.1126/scitranslmed.aav4319.
[33] S.A. Eming, P. Martin, M. Tomic-Canic, Wound repair and regeneration: mechanisms, signaling, and translation, Sci. Transl. Med. 6 (265) (2014) 265sr6, https://doi.org/10.1126/scitranslmed.3009337.
[34] L. Shi, H. Chen, X. Yu, X. Wu, Advanced glycation end products delay corneal epithelial wound healing through reactive oxygen species generation, Mol. Cell. Biochem. 383 (1–2) (2013) 253–259, https://doi.org/10.1007/s11010-013-1773-9.

[35] A. Aljohi, S. Matou-Nasri, D. Liu, N. Al-Khafaji, M. Slevin, N. Ahmed, Momordica charantia extracts protect against inhibition of endothelial angiogenesis by advanced glycation endproducts in vitro, Food Funct. 9 (11) (2018) 5728–5739, https://doi.org/10.1039/c8fo00297e.
[36] E.A. Grice, E.S. Snitkin, L.J. Yockey, D.M. Bermudez, , N.C.S. Program, K.W. Liechty, J.A. Segre, Longitudinal shift in diabetic wound microbiota correlates with prolonged skin defense response, Proc. Natl. Acad. Sci. USA 107 (33) (2010) 14799–14804, https://doi.org/10.1073/pnas.1004204107.
[37] L. Schirmer, P. Atallah, C. Werner, U. Freudenberg, StarPEG-heparin hydrogels to protect and sustainably deliver IL-4, Adv. Healthc. Mater. 5 (24) (2016) 3157–3164, https://doi.org/10.1002/adhm.201600797.
[38] Y. Sato, T. Ohshima, T. Kondo, Regulatory role of endogenous interleukin-10 in cutaneous inflammatory response of murine wound healing, Biochem. Biophys. Res. Commun. 265 (1) (1999) 194–199, https://doi.org/10.1006/bbrc.1999.1455.
[39] A.D. Schoenenberger, H. Tempfer, C. Lehner, J. Egloff, M. Mauracher, A. Bird, J. Widmer, K. Maniura-Weber, S.F. Fucentese, A. Traweger, U. Silvan, J.G. Snedeker, Macromechanics and polycaprolactone fiber organization drive macrophage polarization and regulate inflammatory activation of tendon in vitro and in vivo, Biomaterials 249 (2020), https://doi.org/10.1016/j.biomaterials.2020.120034, 120034.
[40] J. Li, Y. Liu, Y. Zhang, B. Yao, Enhejirigala, Z. Li, W. Song, Y. Wang, X. Duan, X. Yuan, X. Fu, S. Huang, Biophysical and biochemical cues of biomaterials Guide mesenchymal stem cell behaviors, Front. Cell Dev. Biol. 9 (2021), 640388, https://doi.org/10.3389/fcell.2021.640388.
[41] L. Zhu, D. Luo, Y. Liu, Effect of the nano/microscale structure of biomaterial scaffolds on bone regeneration, Int. J. Oral Sci. 12 (1) (2020) 6, https://doi.org/10.1038/s41368-020-0073-y.
[42] Y. He, K. Xu, K. Li, Z. Yuan, Y. Ding, M. Chen, C. Lin, B. Tao, X. Li, G. Zhang, P. Liu, K. Cai, Improved osteointegration by SEW2871-encapsulated multilayers on micro-structured titanium via macrophages recruitment and immunomodulation, Appl. Mater. Today 20 (2020), https://doi.org/10.1016/j.apmt.2020.100673.
[43] E. Saino, M.L. Focarete, C. Gualandi, E. Emanuele, A.I. Cornaglia, M. Imbriani, L. Visai, Effect of electrospun fiber diameter and alignment on macrophage activation and secretion of proinflammatory cytokines and chemokines, Biomacromolecules 12 (5) (2011) 1900–1911, https://doi.org/10.1021/bm200248h.
[44] K. Garg, N.A. Pullen, C.A. Oskeritzian, J.J. Ryan, G.L. Bowlin, Macrophage functional polarization (M1/M2) in response to varying fiber and pore dimensions of electrospun scaffolds, Biomaterials 34 (18) (2013) 4439–4451, https://doi.org/10.1016/j.biomaterials.2013.02.065.
[45] K.A. Barth, J.D. Waterfield, D.M. Brunette, The effect of surface roughness on RAW 264.7 macrophage phenotype, J. Biomed. Mater. Res. 101 (9) (2013) 2679–2688, https://doi.org/10.1002/jbm.a.34562.
[46] L. Lv, Y. Xie, K. Li, T. Hu, X. Lu, Y. Cao, X. Zheng, Unveiling the mechanism of surface hydrophilicity-modulated macrophage polarization, Adv. Healthc. Mater. 7 (19) (2018), e1800675, https://doi.org/10.1002/adhm.201800675.
[47] L. Chen, D. Wang, F. Peng, J. Qiu, L. Ouyang, Y. Qiao, X. Liu, Nanostructural surfaces with different elastic moduli regulate the immune response by stretching macrophages, Nano Lett. 19 (6) (2019) 3480–3489, https://doi.org/10.1021/acs.nanolett.9b00237.
[48] D.Y. Vogel, P.D. Heijnen, M. Breur, H.E. de Vries, A.T. Tool, S. Amor, C.D. Dijkstra, Macrophages migrate in an activation-dependent manner to chemokines involved in neuroinflammation, J. Neuroinflammation 11 (2014) 23, https://doi.org/10.1186/1742-2094-11-23.
[49] A.R. Reeves, K.L. Spiller, D.O. Freytes, G. Vunjak-Novakovic, D.L. Kaplan, Controlled release of cytokines using silk-biomaterials for macrophage polarization, Biomaterials 73 (2015) 272–283, https://doi.org/10.1016/j.biomaterials.2015.09.027.
[50] B. Behm, P. Babilas, M. Landthaler, S. Schreml, Cytokines, chemokines and growth factors in wound healing, J. Eur. Acad. Dermatol. Venereol. 26 (7) (2012) 812–820, https://doi.org/10.1111/j.1468-3083.2011.04415.x.
[51] T. Lucas, A. Waisman, R. Ranjan, J. Roes, T. Krieg, W. Muller, A. Roers, S.A. Eming, Differential roles of macrophages in diverse phases of skin repair, J. Immunol. 184 (7) (2010) 3964–3977, https://doi.org/10.4049/jimmunol.0903356.
[52] N.A. Bhowmick, A. Chytil, D. Plieth, A.E. Gorska, N. Dumont, S. Shappell, M.K. Washington, E.G. Neilson, H.L. Moses, TGF-beta signaling in fibroblasts modulates the oncogenic potential of adjacent epithelia, Science 303 (5659) (2004) 848–851, https://doi.org/10.1126/science.1090922.
[53] K.E. Martin, A.J. Garcia, Macrophage phenotypes in tissue repair and the foreign body response: implications for biomaterial-based regenerative medicine strategies, Acta Biomater. 133 (2021) 4–16, https://doi.org/10.1016/j.actbio.2021.03.038.
[54] K.L. Singampalli, S. Balaji, X. Wang, U.M. Parikh, A. Kaul, J. Gilley, R.K. Birla, P.L. Bollyky, S.G. Keswani, The role of an IL-10/hyaluronan Axis in dermal wound healing, Front. Cell Dev. Biol. 8 (2020) 636, https://doi.org/10.3389/fcell.2020.00636.
[55] J.G. Tidball, Inflammatory processes in muscle injury and repair, Am. J. Physiol. Regul. Integr. Comp. Physiol. 288 (2) (2005) R345–R353, https://doi.org/10.1152/ajpregu.00454.2004.
[56] J. Sapudom, X. Wu, M. Chkolnikov, M. Ansorge, U. Anderegg, T. Pompe, Fibroblast fate regulation by time dependent TGF-beta1 and IL-10 stimulation in biomimetic 3D matrices, Biomater. Sci. 5 (9) (2017) 1858–1867, https://doi.org/10.1039/c7bm00286f.
[57] T.A. Wynn, K.M. Vannella, Macrophages in tissue repair, regeneration, and fibrosis, Immunity 44 (3) (2016) 450–462, https://doi.org/10.1016/j.immuni.2016.02.015.
[58] Y. Zhu, Z. Ma, L. Kong, Y. He, H.F. Chan, H. Li, Modulation of macrophages by bioactive glass/sodium alginate hydrogel is crucial in skin regeneration enhancement, Biomaterials 256 (2020), 120216, https://doi.org/10.1016/j.biomaterials.2020.120216.
[59] B.K. Sun, Z. Siprashvili, P.A. Khavari, Advances in skin grafting and treatment of cutaneous wounds, Science 346 (6212) (2014) 941–945, https://doi.org/10.1126/science.1253836.
[60] A. Vishwakarma, N.S. Bhise, M.B. Evangelista, J. Rouwkema, M.R. Dokmeci, A.M. Ghaemmaghami, N.E. Vrana, A. Khademhosseini, Engineering immunomodulatory biomaterials to tune the inflammatory response, Trends Biotechnol. 34 (6) (2016) 470–482, https://doi.org/10.1016/j.tibtech.2016.03.009.
[61] S. Seetharaman, S. Etienne-Manneville, Cytoskeletal crosstalk in cell migration, Trends Cell Biol. 30 (9) (2020) 720–735, https://doi.org/10.1016/j.tcb.2020.06.004.
[62] C.D. Lawson, A.J. Ridley, Rho GTPase signaling complexes in cell migration and invasion, J. Cell Biol. 217 (2) (2018) 447–457, https://doi.org/10.1083/jcb.201612069.
[63] Y.H. Lin, Y.Y. Zhen, K.Y. Chien, I.C. Lee, W.C. Lin, M.Y. Chen, L.M. Pai, LIMCH1 regulates nonmuscle myosin-II activity and suppresses cell migration, Mol. Biol. Cell 28 (8) (2017) 1054–1065, https://doi.org/10.1091/mbc.E15-04-0218.
[64] S. Bersini, N.K. Lytle, R. Schulte, L. Huang, G.M. Wahl, M.W. Hetzer, Nup93 regulates breast tumor growth by modulating cell proliferation and actin cytoskeleton remodeling, Life Sci. Alliance 3 (1) (2020), https://doi.org/10.26508/lsa.201900623.